





## RESEARCH ARTICLE

10.1029/2019GC008373

## Mantle Dynamics of Western Pacific and East Asia: New Insights from *P* Wave Anisotropic Tomography

Jincheng Ma<sup>1,2</sup> , You Tian<sup>1</sup> , Dapeng Zhao<sup>3</sup> , Cai Liu<sup>1</sup>, and Tingting Liu<sup>4</sup> 

<sup>1</sup>College of Geoexploration Science and Technology, Jilin University, Changchun, China, <sup>2</sup>Department of Earth and Environmental Sciences, Ludwig-Maximilians-Universität München, Munich, Germany, <sup>3</sup>Department of Geophysics, Graduate School of Science, Tohoku University, Sendai, Japan, <sup>4</sup>Geophysical Institute, Karlsruhe Institute of Technology, Karlsruhe, Germany

**Key Points:**

- Depth-varying azimuthal anisotropy is revealed in the Pacific slab and subslab mantle
- Toroidal anisotropy indicates complex mantle flows induced by the Pacific slab tearing under the Izu-Bonin arc
- The results shed new light on intraplate volcanism and mantle dynamics in Western Pacific and East Asia

**Supporting Information:**

- Supporting Information S1

**Correspondence to:**

Y. Tian,  
tianyout@jlu.edu.cn

**Citation:**

Ma, J., Tian, Y., Zhao, D., Liu, C., & Liu, T. (2019). Mantle dynamics of western Pacific and East Asia: New insights from *P* wave anisotropic tomography. *Geochemistry, Geophysics, Geosystems*, 20, 3628–3658. <https://doi.org/10.1029/2019GC008373>

Received 12 APR 2019

Accepted 26 JUN 2019

Accepted article online 2 JUL 2019

Published online 29 JUL 2019

**Abstract** Seismic anisotropy records past and present tectonic deformations and provides important constraints for understanding the structure and dynamics of the Earth's interior. In this work, we use tremendous amounts of high-quality *P* wave arrival times from local and regional earthquakes to determine a high-resolution tomographic model of 3-D *P* wave azimuthal anisotropy down to 1,000-km depth beneath East Asia. Our results show that trench-parallel fast-velocity directions (FVDs) are visible in the shallow portion of the subducting Pacific slab (<80 km), whereas the deeper portion of the Pacific slab mainly exhibits trench-normal FVDs, except for the stagnant slab in the mantle transition zone (MTZ) where obvious NE-SW FVDs are revealed. The FVDs in the subslab mantle change from a subduction-parallel trend at depths of 80–400 km to a subduction-normal trend in the MTZ. Large-scale low-velocity anomalies are revealed beneath the Philippine Sea plate where the FVD is NE-SW. The FVDs along the Izu-Bonin arc and in a slab gap exhibit a striking anticlockwise toroidal trend. All these features may reflect complex 3-D flows in the mantle wedge due to tearing and dehydration processes of the subducting Pacific slab. The subducting Pacific slab is split at ~300-km depth under the Bonin arc and then penetrates into the lower mantle, whereas under East Asia the Pacific slab becomes stagnant in the MTZ and reaches the North-South Gravity Lineament in China. The intraplate volcanoes in East Asia are caused by hot and wet upwelling flows in the big mantle wedge above the stagnant Pacific slab.

### 1. Introduction

In the western Pacific and East Asia region, there exist strong interactions among the Pacific, Okhotsk, Eurasian, and Philippine Sea plates, which have resulted in a very complex and unique geodynamic system (Figure 1a). The western Pacific plate is actively subducting beneath the Okhotsk and Eurasian plates at a rate of ~8–9 cm/yr along the Japan and Kuril trenches and meanwhile subducting beneath the Philippine Sea plate at ~6 cm/yr along the Izu-Bonin and Mariana trenches, whereas the Philippine Sea plate is descending beneath the Eurasian plate at ~3–5 cm/yr along the Nankai Trough and the Ryukyu Trench (Figure 1a; e.g., Seno et al., 1993; DeMets et al., 1994; Bird, 2003; Hayes et al., 2012). Major geological structures and tectonics of East Asia are generally controlled by the development of back-arc extensional systems and the strong interactions between the four lithospheric plates, causing intensive seismic and volcanic activities, and continental lithosphere destruction and deformation. So far, many researchers have used seismic tomography methods to study three-dimensional (3-D) isotropic velocity structures (e.g., Fukao & Obayashi, 2013; Huang & Zhao, 2006; Koulakov, 2011; Lei & Zhao, 2005; Li & van der Hilst, 2010; Ma et al., 2018; Tao et al., 2018; Tian et al., 2009; Zhao, 2004), azimuthal and radial anisotropies (e.g., Huang et al., 2014; Ishise & Oda, 2005; Liu et al., 2013; Liu & Zhao, 2017; Niu et al., 2016; Wang et al., 2014; Wang & Zhao, 2008; Wei et al., 2015), and attenuation structures (e.g., Liu et al., 2014; Liu & Zhao, 2015; Wang, Zhao, Liu, Chen, & Li, 2017; Wang, Zhao, Liu, & Li, 2017) beneath East Asia, which have greatly improved our understanding of the structure and dynamic evolution of this broad region.

As a characteristic feature of the Earth's interior structure, seismic anisotropy refers to the directional dependence of seismic velocity and particle motion polarizations, which can provide important constraints on the tectonic stress and deformation in the lithosphere and mantle to better understand the structure and dynamic processes in the Earth (e.g., Becker et al., 2012; Fouch & Rondenay, 2006; Karato et al., 2008; Long, 2013; Savage, 1999; Zhao et al., 2016). The major causes of seismic anisotropy are shape-preferred

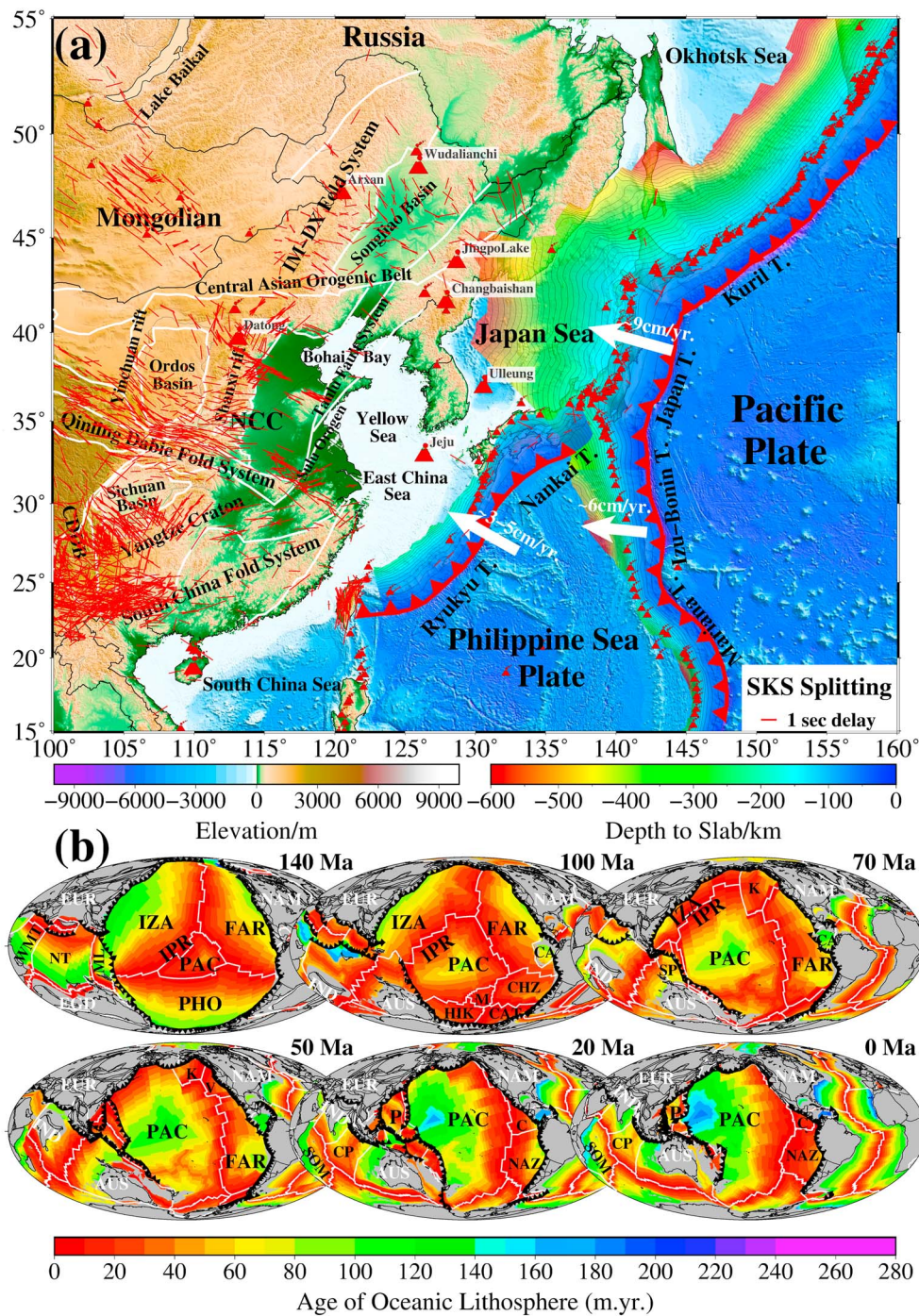


**Figure 1.** (a) A map showing the surface topography and major tectonic features of the study region. A color scale for the elevation is shown below the map. The red sawtooth lines show major plate boundaries, and the white solid lines denote main block boundaries or large fault zones. The color contour lines show depths to the upper boundaries of the subducting Pacific and Philippine Sea slabs with an interval of 20 km (Hayes et al., 2012), whose scale is shown below the map. The white bold arrows indicate motion directions of the Pacific and Philippine Sea plates relative to the Eurasian plate. The short red lines show the fast directions from the SKS splitting measurements in East Asia compiled by Wüstefeld et al. (2009). The length of the short red lines denotes the delay time of SKS splitting, whose scale is shown in the lower right inset. The red triangles denote active volcanoes. NCC, the North China Craton; CDDB, the Chuandian Diamond Block. (b) Age-area distributions of oceanic crust at 140, 100, 70, 50, 20, and 0 Ma (modified from Müller et al., 2016). The black sawtooth lines delineate subduction zones, whereas the white lines indicate mid-ocean ridges and transform faults. AUS, the Australian plate; C, the Cocos plate; CA, the Caribbean plate; CAT, the Catequil plate; CHZ, the Chasca plate; CP, the Capricorn plate; EGD, East Gondwana; EUR, the Eurasian plate; FAR, the Farallon plate; HIK, the Hikurangi Plateau; IND, the Indian plate; IPR, the Izanagi-Pacific Ridge; IZA, the Izanagi plate; K, the Kula plate; M, the Manihiki Plateau; ML, the Proto-Molucca Plate; NAM, the North American plate; NAZ, the Nazca plate; NT, the Neo-Tethys Ocean; P, the Philippine Sea plate; PAC, the Pacific plate; PHO, the Phoenix plate; SOM, the Somali plate; SP, the Sepik plate; V, the Vancouver plate; and WMT, the West Meso-Tethys Ocean.



orientation (SPO) and lattice-preferred orientation (LPO) of the Earth's interior materials (e.g., Becker, 2011; Fouch & Rondenay, 2006). Seismic anisotropy in the lithosphere, especially in the upper crust, is mainly caused by the SPO. The upper crust is dominated by brittle deformation, and its anisotropy is generally caused by crack alignment that may be indicative of crustal stress (Crampin et al., 1984, Crampin & Chastin, 2003). In the extensional tectonic regime, the fast velocity direction (FVD) of azimuthal anisotropy is parallel to the direction of extension and normal to tectonic stress (e.g., Savage, 1999; Silver, 1996). However, in the compressional tectonic regime, the FVD is usually parallel to strikes of active faults and orogens (e.g., Nicolas, 1993; Savage, 1999; Silver, 1996; Silver & Chan, 1991). The SPO also plays a role in shallow, extensional lithospheric domains, such as in mid-ocean spreading centers, subduction zones, and intracontinental rifts (e.g., Becker, 2011; Holtzman et al., 2003). Fouch and Rondenay (2006) suggested that SPO is a local crustal phenomenon with less broad-scale effect on most seismic anisotropy observations beneath stable continental interiors with a thick lithosphere. Seismic anisotropy in the upper mantle is induced mainly by the LPO of anisotropic mantle minerals, primarily olivine (e.g., Holtzman et al., 2003; Karato & Wu, 1993; Mainprice & Silver, 1993; Nicolas & Christensen, 1987). In the deeper mantle, other minerals may contribute to anisotropy, including wadsleyite in the mantle transition zone (MTZ), and perovskite, post-perovskite, and/or ferropericlase in the lowermost mantle (Long & Silver, 2008). The absolute plate motion and mantle flow in subduction zones can result in alignment of olivine and other minerals, and then the fast axis of crystals generally becomes parallel to the direction of the absolute plate motion and mantle flow.

Shear wave splitting (SWS) refers to a phenomenon that an incident shear wave splits into two orthogonal polarized shear waves with different velocities when passing through an anisotropic medium. Long-period core phases, such as SKS, SKKS, and PKS, are the most popular phases used in SWS studies to probe anisotropic structure in the crust and upper mantle (e.g., Fouch & Rondenay, 2006; Long & Silver, 2008). Measuring SWS has been an effective and popular tool to characterize seismic anisotropy in the Earth (e.g., Eakin et al., 2015, 2016; Savage, 1999; Silver, 1996). So far, many researchers have used SWS methods to study the anisotropy in East Asia (e.g., Chen et al., 2015; Chen, Niu, et al., 2017; Huang, Wang, et al., 2011; Huang, Zhao, & Wang, 2011; Huang, Wang, et al., 2015; Zhao & Xue, 2010). However, SWS measurements generally lack depth resolution because the observed splitting time just reflects an integrated effect along the near-vertical raypath to the surface, and so the interpretation of SWS results with regard to the mantle structure and dynamics is usually not unique. Fortunately, *P* wave anisotropic tomography can well overcome the drawback of SWS measurements, because the *P* wave method has a good vertical resolution and is able to determine 3-D variations of seismic anisotropy (e.g., Eberhart-Phillips & Henderson, 2004; Ishise & Oda, 2005; Liu & Zhao, 2017; Tian & Zhao, 2012, 2013; Wang & Zhao, 2008, 2013; Zhao et al., 2016). Although many studies have been made on seismic anisotropy in East Asia as mentioned above, most of the previous results are limited to the upper mantle (< ~400-km depth) due to the limited ray coverage in the deeper mantle in those studies. Hence, the fine-scale 3-D anisotropy structure of the entire lithosphere and mantle beneath East Asia has not been investigated yet, which undoubtedly hinders our understanding of the mantle structure and dynamic processes of this region.

In this study, we determine high-resolution 3-D isotropic and anisotropic velocity images of the crust and mantle down to 1,000-km depth beneath the western Pacific and East Asian region. We have used a large number of high-quality *P* wave arrival time data from many local and regional earthquakes compiled by the International Seismological Center (ISC), the Japanese Kiban Seismic Network, and the China Earthquake Data Center. Our robust results have a high enough resolution in the lithosphere, asthenosphere, MTZ, and the uppermost lower mantle, which shed important new light on the detailed mantle structure, the fate of the subducting slabs and their effects on the intraplate seismicity, Cenozoic volcanism, and continental deformation in East Asia. Hence, the present results will improve our understanding of the 3-D seismic structure, tectonic evolution, and active subduction dynamics of the western Pacific tectonic domain.

## 2. Data and Method

### 2.1. Data

We used three sets of high-quality *P* wave arrival time data, including the ISC data from January 1980 to December 2013 (<http://www.isc.ac.uk>), the Japanese Kiban Seismic Network data from June 2002 to

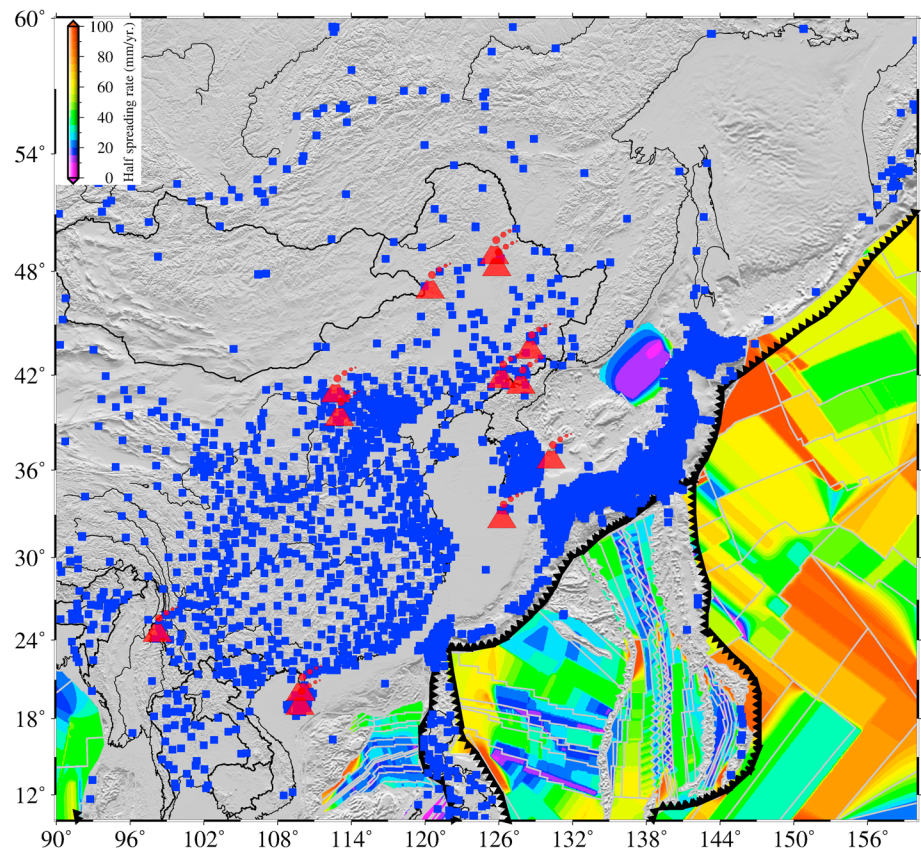


**Figure 2.** Distribution of the over 3,000 seismic stations (blue squares) used in this study. The colors denote the half-spreading rate of ocean floor from Müller, Sdrolias, Gaiña, and Roest (2008), whose scale is shown in the upper left inset. The red triangles denote active intraplate volcanoes.

December 2016 (<http://www.hinet.bosai.go.jp>), and the China Earthquake Data Center data from January 1990 to March 2016 (<http://data.earthquake.cn>). Before combining the three data sets, we first eliminated those overlapping and inconsistent events, because sometimes the arrival time data from the same event to the same stations are considerably different in different databases. For the events that are located in mainland China and were not reported by ISC, we used their hypocentral parameters determined by the Chinese seismic networks. Then we selected the final events for tomographic inversion in this study with the following criteria: (a) Each event was recorded at more than 10 seismic stations; (b) the earthquake magnitude is greater than  $M$  3.0; (c) the study volume is divided into  $0.1^\circ \times 0.1^\circ \times 5$ -km blocks and only one earthquake is selected in each block, which has the maximum number of  $P$  wave arrivals and the minimum location uncertainty; (d) the absolute value of the traveltime residual is smaller than 5.0 s (the traveltime residual is obtained by subtracting the theoretical traveltime from the observed travel time, and the theoretical traveltime is calculated for the IASP91 model; Kennett & Engdahl, 1991; Figures S1a–S1c in the supporting information). We carefully processed a huge amount of data, and our final data set contains a total of 1,868,800  $P$  wave arrival times of 84,777 local and regional earthquakes recorded at more than 3,000 seismic stations in the study region (Figures 2 and 3). These data are inverted for 3-D  $P$  wave velocity ( $V_p$ ) image and anisotropic structure beneath the study region. The traveltime residuals are reduced significantly after the tomographic inversion (Figures S1c, S1d, S1g, and S1h). About 41.5% of the data have epicentral distances of  $18^\circ$  to  $50^\circ$  with takeoff angles of  $17^\circ$ – $70^\circ$  (Figures S1e and S1f). Hence, many  $P$  wave rays penetrate deeply in the mantle and can well constrain the structure of the MTZ and uppermost lower mantle.

Comparing with many previous studies (e.g., Huang et al., 2014; Huang & Zhao, 2006; Koulakov, 2011; Li & van der Hilst, 2010; Wei et al., 2012, 2016), we have used much more seismic stations in mainland China and a greater number of seismic events (Figures 2 and 3), in particular, many deep earthquakes with a large



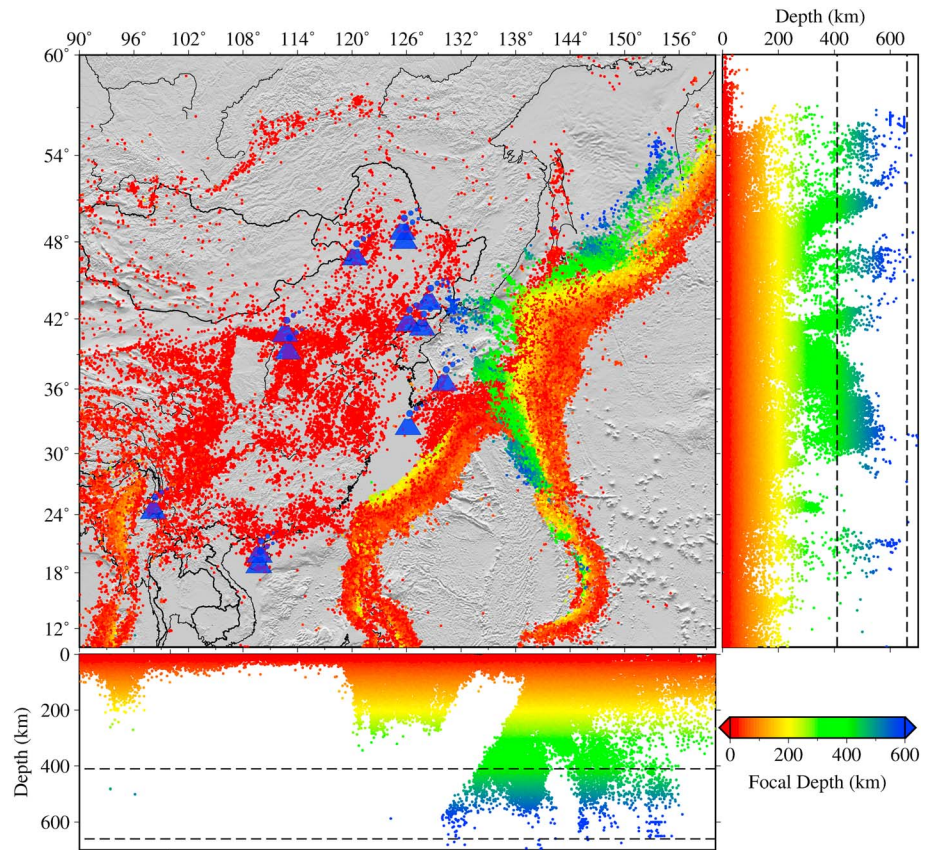


**Figure 3.** Distribution of the 84,777 local and regional earthquakes (color dots) used in this study. The colors denote the focal depths whose scale is shown at the lower right corner. The blue triangles denote active intraplate volcanoes.

number of arrival time data, which can greatly improve the ray coverage in the study volume and so lead to a higher-resolution and more robust tomographic model.

## 2.2. Method

We use the method of azimuthal anisotropy tomography (Wang & Zhao, 2008, 2013) to invert the  $P$  wave arrival times of local and regional earthquakes for 3-D isotropic  $V_p$  and  $P$  wave azimuthal anisotropic structures of the study volume that is in a latitude range of  $10^{\circ}$ – $60^{\circ}$ N, longitude range of  $90^{\circ}$ – $160^{\circ}$ E, and a depth range of 0–1,000 km. In a weak anisotropic medium with a horizontal hexagonal symmetry axis,  $P_n$  wave slowness can be approximately expressed as a function of the azimuth of  $P$  wave propagation ( $\phi$ ; e.g., Backus, 1965; Raitt et al., 1969; Hearn, 1996; Eberhart-Phillips & Henderson, 2004):

$$S(\phi) = S_0(1 + A \cos 2\phi + B \sin 2\phi) \quad (1)$$

where  $S$  is the total slowness,  $S_0$  is the azimuthal average slowness,  $A$  and  $B$  are two azimuthal anisotropy parameters, and  $\phi$  is the raypath azimuth.

Eberhart-Phillips and Henderson (2004) modified equation (1) to the following equation to adapt to general  $P$  wave rays with any incident angle  $i$ :

$$S(\phi) = S_0 \left[ 1 - \cos^2 i \sqrt{A^2 + B^2} + \sin^2 i (A \cos 2\phi + B \sin 2\phi) \right] \quad (2)$$

Thus, traveltimes residual  $r_{ij}$  from the  $j$ th event to the  $i$ th station can be written as

$$r_{ij} = T_{ij}^{\text{obs}} - T_{ij}^{\text{cal}} = \left(\frac{\partial T}{\partial \varphi}\right)_{ij} \Delta \varphi_j + \left(\frac{\partial T}{\partial \lambda}\right)_{ij} \Delta \lambda_j + \left(\frac{\partial T}{\partial h}\right)_{ij} \Delta h_j + \Delta T_{0j} + \sum_k \frac{\partial T}{\partial V_k} \Delta V_k + \sum_l \left(\frac{\partial T}{\partial A_l} \Delta A_l + \frac{\partial T}{\partial B_l} \Delta B_l\right) + E_{ij} \quad (3)$$

where  $T_{ij}^{\text{cal}}$  is the theoretical traveltime;  $\varphi_j$ ,  $\lambda_j$ ,  $h_j$ , and  $T_{0j}$  are latitude, longitude, focal depth, and origin time of the  $j$ th event;  $V_k$  is isotropic velocity at the  $k$ th node of the 3-D isotropic grid arranged in the study volume;  $A_l$  and  $B_l$  are anisotropic parameters at the  $l$ th node of the 3-D anisotropic grid arranged in the study volume; and  $E_{ij}$  is higher-order terms and errors of the data.

The observation equation (3) relates an observed traveltime residual to the 3-D isotropic and anisotropic  $V_p$  parameters, as well as hypocentral parameters.  $\partial T/\partial \varphi$ ,  $\partial T/\partial \lambda$ , and  $\partial T/\partial h$  are partial derivatives of traveltime with respect to the hypocentral parameters (for details, see Engdahl & Lee, 1976), and  $dT/dV$  is partial derivatives of traveltime with respect to the velocity at each isotropic grid node (Thurber, 1983):

$$\frac{\partial T}{\partial V} = -\frac{d}{V^2} \quad (4)$$

where  $d$  is length of a ray segment.

$\partial T/\partial A$  and  $\partial T/\partial B$  are partial derivatives of traveltime with respect to  $A$  and  $B$  at each anisotropic grid node (e.g., Eberhart-Phillips & Henderson, 2004; Wang & Zhao, 2008):

$$\frac{\partial T}{\partial A} = \frac{d}{V} \cdot \left( -\cos^2 i \cdot \frac{A}{\sqrt{A^2 + B^2}} + \sin^2 i \cdot \cos 2\phi \right) \quad (5)$$

$$\frac{\partial T}{\partial B} = \frac{d}{V} \cdot \left( -\cos^2 i \cdot \frac{B}{\sqrt{A^2 + B^2}} + \sin^2 i \cdot \sin 2\phi \right) \quad (6)$$

We set up two 3-D grid nets in the study volume with a grid interval of  $1.0^\circ$  in the longitude and latitude directions and at depths of 10, 25, 50, 80, 160, 240, 320, 400, 480, 560, 640, 720, 800, 900, and 1,000 km. One grid net is adopted to express the 3-D isotropic  $V_p$  structure, and the other grid net is adopted to express the 3-D anisotropic  $V_p$  structure. A modified IASP91 velocity model (Kennett & Engdahl, 1991, Figure S2) is adopted as the 1-D starting  $V_p$  model for the mantle, and traveltimes in the crust are corrected using the CRUST1.0 model (Laske et al., 2013). Perturbations of the isotropic and anisotropic  $V_p$  parameters at the 3-D grid nodes are taken as unknown parameters. The perturbation at any point in the model is calculated by trilinearly interpolating the perturbations at the eight grid nodes surrounding that point. For example,  $V_k$ ,  $A_l$ , and  $B_l$  are defined at  $(\varphi, \lambda, h)$ , and  $F(\varphi, \lambda, h)$  is calculated by using a linear interpolation function as follows:

$$F(\varphi, \lambda, h) = \sum_{i=1}^2 \sum_{j=1}^2 \sum_{k=1}^2 F(\varphi_i, \lambda_j, h_k) \left[ \left( 1 - \frac{|\varphi - \varphi_i|}{|\varphi_2 - \varphi_1|} \right) \left( 1 - \frac{|\lambda - \lambda_j|}{|\lambda_2 - \lambda_1|} \right) \left( 1 - \frac{|h - h_k|}{|h_2 - h_1|} \right) \right] \quad (7)$$

where  $\varphi_i$ ,  $\lambda_j$ , and  $h_k$  represent the coordinates of the eight grid nodes surrounding the point  $(\varphi, \lambda, h)$ . We use the robust and efficient 3-D ray-tracing technique of Zhao et al. (1992) in a spherical Earth that combines the pseudobending algorithm (Um & Thurber, 1987) and Snell's law to compute theoretical traveltimes and ray-paths. The station elevations and surface topography are also taken into account in the 3-D ray tracing. The calculated traveltimes are further corrected for the Earth's ellipticity following Kennett and Gudmundsson (1996).

We used the iterative conjugate-gradient Least Squares Minimal Residual (LSMR) algorithm, which is based on the Golub-Kahan bidiagonalization process and can converge faster and safer than the commonly used LSQR algorithm (Fong & Saunders, 2011; Paige & Saunders, 1982), with norm damping  $\lambda$  and gradient damping  $\mu$  (for smoothing) to solve the large and sparse system of observation equation (3) by minimizing (e.g., Wei et al., 2016)

$$\|G \cdot m - d\|^2 + \lambda^2 \|m\|^2 + \mu^2 \|L \cdot m\|^2 \quad (8)$$

where the model vector  $m$  represents perturbations to the hypocentral parameters, as well as isotropic  $V_p$  parameter ( $\Delta V$ ) and anisotropic parameters ( $\Delta A$ ,  $\Delta B$ ), and the data vector  $d$  represents raw residuals ( $r_{ij}$ )



between observed and predicted traveltimes for local and regional events;  $G$  is the partial-derivative matrix composed of partial differential coefficients that links up the vector  $m$  and  $d$ , sampled by the seismic ray paths. To overcome the highly ill-conditioned and instability problems during tomographic inversion, we have to invoke some regularization methods on the ill-conditioned system with additional constraints, such as damping and smoothing regularizations. In equation (8), the second term is the magnitude of model vector itself with a damping factor  $\lambda$  to suppress the overreaction of the model norm; the third term represents the smoothing constraint, where  $L$  is 3-D finite difference approximation to the Laplacian operator applied over all model grid nodes in our present study (Lees & Crosson, 1989; Shearer, 2009) in charge of the roughness over the model space, and the coefficient  $\mu$  is a factor to control the level. Each row of  $L$  is given by the difference between the target grid node and the weighted average of the adjacent nodes. For example, in the 3-D model the Laplacian operator is expressed as following formula for the  $(i, j, k)$  grid node:

$$\begin{cases} \Delta V_{i,j,k} - S_{Vv}(\Delta V_{i,j,k-1} + \Delta V_{i,j,k+1}) - S_{Vh}(\Delta V_{i-1,j,k} + \Delta V_{i+1,j,k} + \Delta V_{i,j-1,k} + \Delta V_{i,j+1,k}) = 0 \\ \Delta A_{i,j,k} - S_{Av}(\Delta A_{i,j,k-1} + \Delta A_{i,j,k+1}) - S_{Ah}(\Delta A_{i-1,j,k} + \Delta A_{i+1,j,k} + \Delta A_{i,j-1,k} + \Delta A_{i,j+1,k}) = 0 \\ \Delta B_{i,j,k} - S_{Bv}(\Delta B_{i,j,k-1} + \Delta B_{i,j,k+1}) - S_{Bh}(\Delta B_{i-1,j,k} + \Delta B_{i+1,j,k} + \Delta B_{i,j-1,k} + \Delta B_{i,j+1,k}) = 0 \end{cases} \quad (9)$$

where  $S_{Vv}$  and  $S_{Vh}$ ,  $S_{Av}$  ( $= S_{Bv}$ ) and  $S_{Ah}$  ( $= S_{Bh}$ ) are the vertical and horizontal smoothing parameters for the isotropic  $Vp$  and anisotropy, respectively.

We first searched for the optimal value of the damping parameter on the basis of the tradeoff curve between the norm of the tomographic solution and the final root-mean-square (RMS) traveltime residual by an extensive series of inversions. Then we selected the optimal value of the smoothing parameters with the same approach. We found that the best damping parameter is  $\lambda = 10.0$  and  $\mu = 40.0$ , and the best vertical and horizontal smoothing parameters are  $S_{Vv} = 0.0005$  and  $S_{Vh} = 0.0002$ , and  $S_{Av} = S_{Bv} = 0.0003$  and  $S_{Ah} = S_{Bh} = 0.0001$  for the present data set and model parameterization, which lead to the balance between the reduction of the RMS traveltime residual and the smoothness of the final 3-D  $Vp$  model (Figure S3).

When the anisotropic parameters  $A$  and  $B$  are finally determined, the FVD  $\psi$  and the amplitude  $\alpha$  of  $Vp$  azimuthal anisotropy can be expressed as follows (Wang & Zhao, 2008):

$$\psi(A, B) = \begin{cases} \frac{1}{2} \tan^{-1} \left( \frac{B}{A} \right) + \begin{cases} \frac{\pi}{2}, A > 0 \\ 0, A < 0 \end{cases} \\ \begin{cases} -\frac{\pi}{4}, B > 0 \\ \frac{\pi}{4}, B < 0 \end{cases} \end{cases}, A = 0 \quad (10)$$

$$\alpha(A, B) = \frac{\sqrt{A^2 + B^2}}{1 - (A^2 + B^2)} \times 100\% \quad (11)$$

### 3. Analysis and Results

#### 3.1. Seismic Ray Coverage

Figure S4 shows the distribution of hit counts (number of rays passing around each grid node in the model) at every grid node in 14 depth layers. A large number of rays sample the upper mantle, MTZ and uppermost lower mantle beneath the subduction zones, for example, the Japan Islands, Kuril, Izu-Bonin, Ryukyu, and the Japan Sea, indicating that the seismic structure there can be well recovered. The hit counts are generally  $>1,000$  at 25–800-km depths (Figures S4a–S4l), because shallow and deep earthquakes actively occurred there and over 2,000 evenly distributed stations are located on the Japan Islands. Beneath northeast, north, and south China, the hit counts at these depths usually range from 100 to 10,000. At the shallow depths (i.e., 25, 50, 80, 160, and 240 km), eastern China is well covered by seismic rays and the hit counts are generally 100–1,000 (Figures S4a–S4e). At the greater depths (i.e., 320, 400, 480, 560, 640, 720, and 800 km), the hit counts are mostly  $>1,000$  (Figures S4f–S4l), which mainly benefits from the dense network of permanent seismic stations in eastern China and the regional earthquakes with epicentral distances of  $20^\circ$ – $50^\circ$ , and

those rays penetrate deeply in the mantle and well constrain the structure of the MTZ and uppermost lower mantle. In the other regions, such as Mongolia and Russia except for the areas of Lake Baikal, the hit counts are mostly <1,000 (Figures S4a–S4d) at the shallow depths due to the lack of earthquakes and stations, whereas as depth increases, these regions are better sampled by the rays and the hit counts are generally >1,000. In the tomographic inversion scheme (Zhao et al., 1992, 1994), if the hit count at a grid node is <20, the grid node is taken away from the final inversion so that a robust 3-D  $V_p$  model can be obtained. As a whole, the ray coverage is very good in most of the study volume, enabling us to well resolve the 3-D isotropic and anisotropic  $V_p$  structures there.

### 3.2. Checkerboard Resolution Tests

To evaluate the resolution and robustness of the obtained tomographic model with our data set, we carried out checkerboard resolution test (CRT) before describing the main features of the tomographic results. In the input models of CRT for  $V_p$  isotropic and azimuthal anisotropy models, we first alternately assigned positive and negative  $V_p$  anomalies of 2% to the 3-D grid nodes of the isotropic grid net, and we assigned anomalies of  $\pm 2\%$  to the anisotropic parameters  $A$  and  $B$  at the grid nodes of the anisotropic grid net, which represent the FVDs at two adjacent grid nodes perpendicular to each other ( $22.5^\circ$  and  $112.5^\circ$ ) with an anisotropic amplitude of  $\sim 2.8\%$ . Then we calculated synthetic data for the input checkerboard model, which are then inverted to obtain a recovered image of the checkerboard model. The numbers of seismic stations, events, raypaths, and the 1-D velocity model in the synthetic data are the same as those in the observed data. Random noise ( $-0.2$  to  $+0.2$  s) with a Gaussian distribution in a standard deviation of 0.1 s is added to the synthetic data for simulating the picking errors in the observed data. We used the same inversion algorithm and parameters as for the observed data to invert the synthetic data.

Figures 4 and 5 show the recovered CRT results for the isotropic  $V_p$  and  $P$  wave azimuthal anisotropy with a lateral grid interval of  $1.0^\circ$  at 14 depth layers. The optimal grid interval ( $1.0^\circ$ ) is found by comparing many CRT results with different grid intervals in the horizontal direction. As a whole, the input  $V_p$  anomalies are well recovered under most parts of our study region, including eastern China, the Korean Peninsula, the Japan Sea, and the Japan Islands, whereas the checkerboard pattern is recovered less well in the Philippine Sea at the shallow depths (Figures 4a–4d) and poorly recovered in the Pacific Ocean (Figures 4a–4l) because of the lack of seismic stations and local earthquakes there, which is also consistent with the distribution of ray coverage (Figure S4). Compared to the isotropic  $V_p$  tomography, a much better azimuthal coverage of rays is required to resolve the anisotropic  $V_p$  structure. We adopt the parameter  $R$  to evaluate the degree of recovery for  $V_p$  azimuthal anisotropy (Huang & Zhao, 2013):

$$R = \frac{\alpha}{\alpha_0} \cdot |\cos(\psi - \psi_0)| \quad (12)$$

where  $(\alpha_0, \psi_0)$  and  $(\alpha, \psi)$  are the input and recovered anisotropic parameters, respectively. When both  $\alpha$  and  $\psi$  are completely recovered,  $R$  equals 1; by contrast, when the recovered amplitude  $\alpha$  is 0 or the recovered  $\psi$  is perpendicular to the input  $\psi_0$ ,  $R$  equals 0. We consider that  $V_p$  azimuthal anisotropy is well recovered when  $R$  is  $\geq 0.5$  at the corresponding grid nodes. Figure 5 shows that the input checkerboard pattern of  $V_p$  anisotropy is well recovered under most parts of the study region, except for the area to the west of the North-South Gravity Lineament (NSGL; Figures 5a–5f), the Philippine Sea (Figures 5a–5d), and the Pacific Ocean (Figures 5a–5l) where the azimuthal ray coverage is not good due to low seismicity and few seismic stations. In the following, we focus on the areas where the tomographic resolution is good.

### 3.3. Tomographic Results

Figure 6 shows plan views of 3-D  $V_p$  azimuthal anisotropy together with isotropic  $V_p$  variation at 14 layers down to 1,000-km depth under the study region. The most significant features of the upper mantle images are continuous high-velocity (high-V) anomalies spreading westward far behind the oceanic trenches, which reflect the subducting Pacific and Philippine Sea slabs. Intermediate-depth and deep earthquakes occurred actively in the high-V subducting slabs. In the Izu-Bonin region, the subducting Pacific slab is split at  $\sim 35^\circ$  north latitude in the upper mantle. The southern Pacific slab is directly penetrating into the lower mantle with associated deep seismicity (e.g., Fukao et al., 2001; Obayashi et al., 2009; Zhao et al., 2017), whereas the northern Pacific slab becomes horizontal and stagnant in the MTZ in good coincidence with the



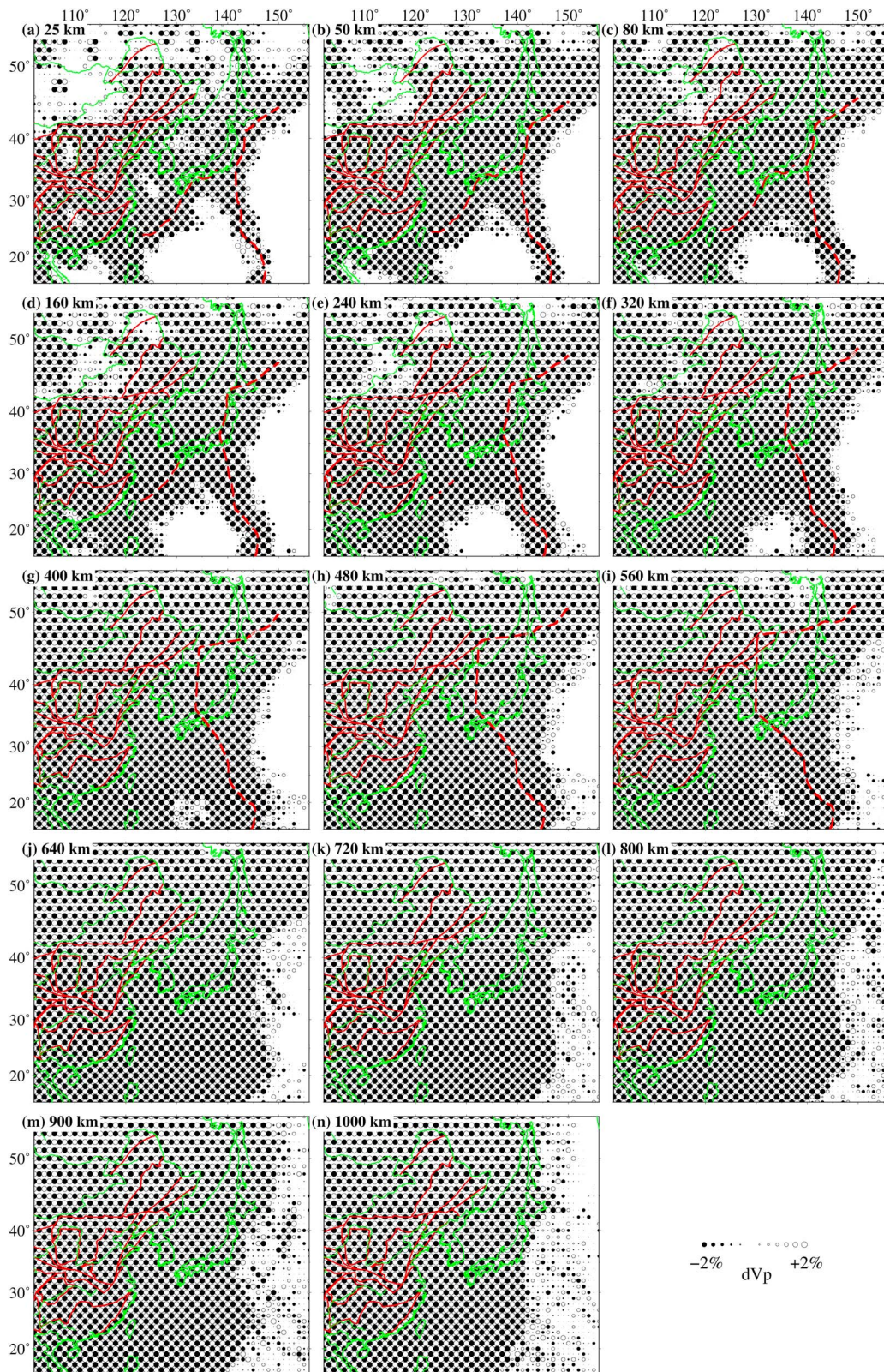


**Figure 4.** Map views showing results of a checkerboard resolution test with a lateral grid interval of  $1^\circ$  in the longitudinal and latitudinal directions. The layer depth is shown in the upper left inset. The solid and open circles denote negative and positive velocity perturbations (%), respectively, whose scale is shown at the lower right corner. The red dashed lines show the upper boundaries of the subducting Pacific and Philippine Sea slabs at each depth. The red solid lines denote the main tectonic boundaries or large fault zones.



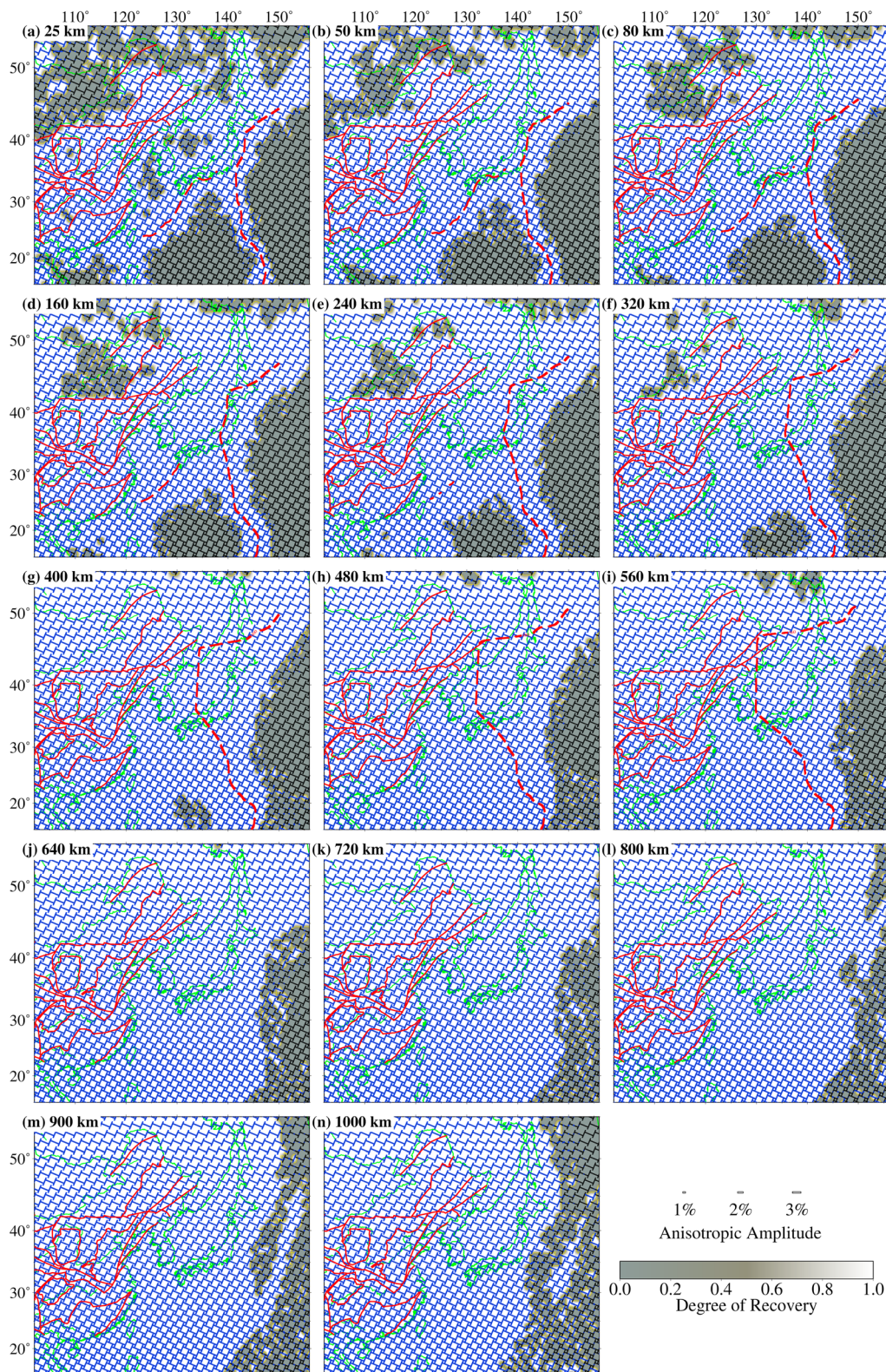


**Figure 5.** Map views showing results of a checkerboard resolution test for  $P$  wave azimuthal anisotropy tomography with a lateral grid interval of  $1^\circ$  in the longitudinal and latitudinal directions. The layer depth is shown in the upper left inset. The thin black bars show the FVDs in the input model, whereas the thick blue bars denote the FVDs recovered after the tomographic inversion. The orientation and length of the bars represent the FVD and the anisotropic amplitude, respectively. The scale for the anisotropic amplitude is shown at the lower right corner. The gray color denotes the degree of recovery ( $R$ ) of the  $P$  wave anisotropy (see text for details), whose scale is shown at the lower right corner. The other labeling is the same as that in Figure 4.



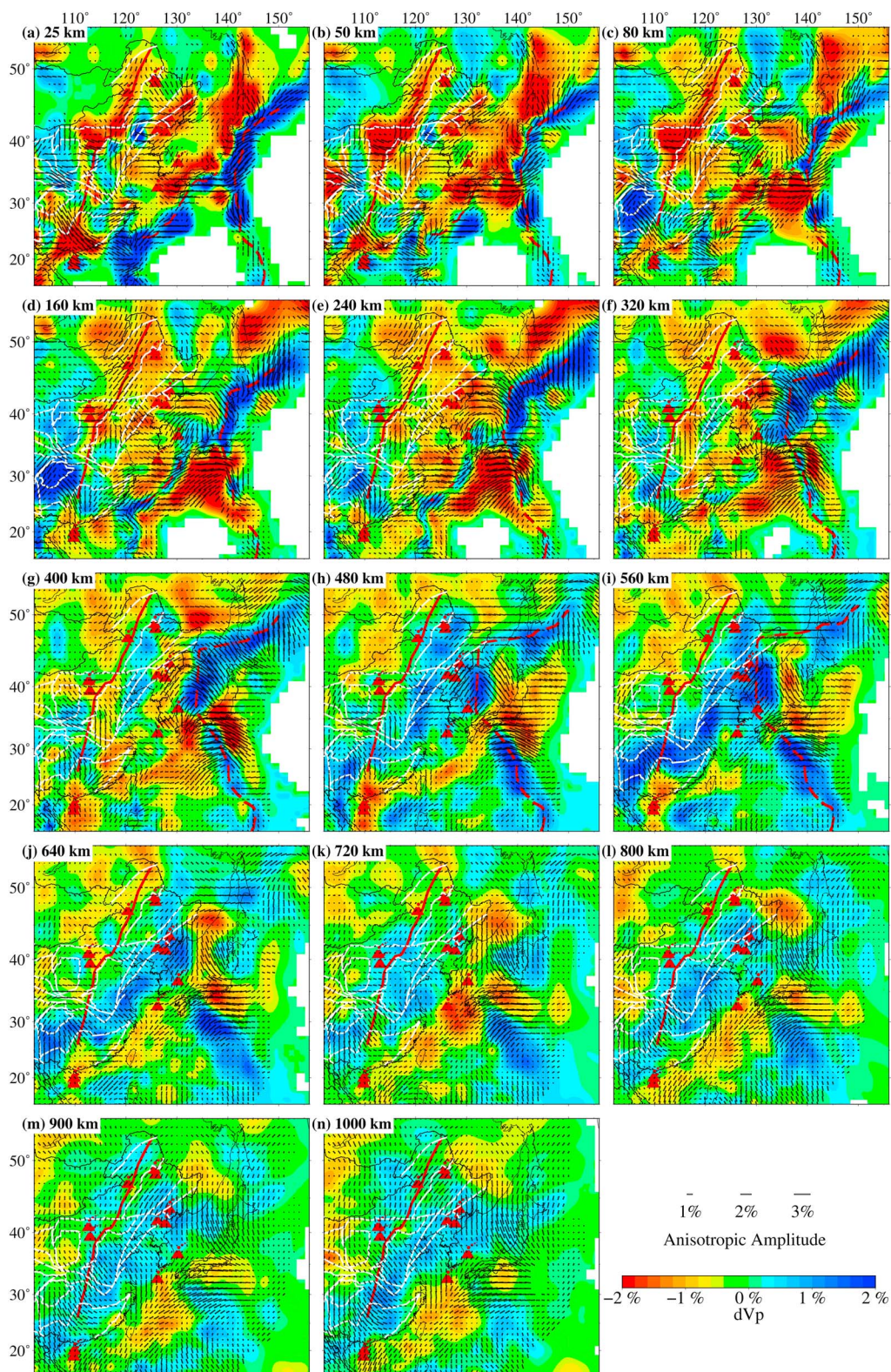


**Figure 6.** Map views of isotropic  $V_p$  and azimuthal anisotropy results. The layer depth is shown in the upper left inset. The red and blue colors denote low and high isotropic  $V_p$  perturbations, respectively. The orientation and length of the short black bars represent the FVD and the anisotropic amplitude, respectively. The scales for the isotropic  $V_p$  perturbation (in %) and anisotropic magnitude are shown at the lower right corner. The red dashed lines show the upper boundaries of the subducting Pacific and Philippine Sea slabs at each depth. The red solid line denotes the NSGL. The white lines denote the main tectonic boundaries or large fault zones. The red triangles denote active intraplate volcanoes.

NSGL in east China. Under the Nankai and Ryukyu arcs, the subducting Philippine Sea slab is also visible as a high- $V$  zone with intermediate-depth earthquakes occurring down to  $\sim 250$ -km depth. However, the subducting Philippine Sea slab is young and has a thickness of  $\sim 50$  km or less, and the obtained slab images may suffer strong smearing effect from the slab low-velocity (low- $V$ ) anomalies. In the Ryukyu arc, there exist much fewer seismic stations and less deep seismicity than those in the Japan Islands. Hence, the Philippine Sea slab is less well imaged as the Pacific slab.

Beneath the Philippine Sea, large-scale and strong low- $V$  anomalies are revealed at depths of 50 to 800 km, which may be associated with the Kyushu-Palau Ridge (Seno et al., 1993) in the crust and the shallow upper mantle, and the dehydration and tearing processes of the subducting Pacific slab in the deep mantle. Clear low- $V$  anomalies are also imaged at depths of 160 to 800 km under the subducting Pacific slab in the Izu-Bonin and Japan arcs, which should be closely related to the Pacific plate deep subduction and complex corner flows in the Pacific slab mantle. In the crust and upper mantle, significant low- $V$  anomalies also exist broadly under the Japan Islands, west Pacific marginal seas, and east China, and with the increasing depth the low- $V$  zones extend gradually toward the NSGL downward to a depth of  $\sim 400$  km. At depths of 480–640 km, broad high- $V$  anomalies are visible under eastern China, which is consistent with the suggestion about the existence of the stagnant Pacific slab in the MTZ under East China (e.g., Fukao et al., 2001; Huang & Zhao, 2006; Wei et al., 2012; Zhao, 2004). It is remarkable that the north-south extent of the stagnant Pacific slab in the MTZ is far greater than that of the Japan trench, suggesting that before the tearing of the Pacific slab beneath the Izu-Bonin arc, there ever existed a link between the stagnant Pacific slab under south China and the subducting Pacific slab under the Izu-Bonin arc. Prominent high- $V$  anomalies appear in the lower mantle under the stagnant Pacific slab beneath East China, which might be pieces of the Izanagi/Pacific slab or ancient continental lithosphere collapsing down to the lower mantle (e.g., Zhao, 2004).

As suggested by Maggi et al. (2006), it is difficult to compare the anisotropic amplitudes among different models due to strong effects of the damping and smoothing regularizations adopted in the different tomographic inversion schemes. Therefore, in the following we mainly focus our discussion on the FVD depth variations of  $V_p$  azimuthal anisotropy in the study region. The most important feature of Figure 6 is that the FVDs in the Pacific slab mantle beneath the Japan Arc show striking variations from the upper mantle down to the lower mantle. The FVDs seem to rotate  $\sim 90^\circ$  in the MTZ under the subducting Pacific slab, that is, from the subduction-parallel trend in the upper mantle to the subduction-normal trend in the MTZ and uppermost lower mantle. The subducting Pacific slab mainly exhibits trench-parallel FVDs at 25–80-km depths, whereas trench-normal FVDs are generally revealed at 160–400-km depths, and at 480-km depth the FVDs change abruptly to NE-SW (trench parallel), which may be caused by multiple metamorphism of the subducting Pacific slab as it continuously descends into the deep mantle, and strong internal deformation of the stagnant slab in the MTZ (e.g., Wei et al., 2015). Beneath the Philippine Sea plate and the Izu-Bonin region, complex FVDs appear at 25–800-km depths. The FVDs tend to become nearly E-W at 25–160-km depths between the Nankai and Izu-Bonin trenches (Figures 6a–6d), whereas in the deeper areas under most parts of the Philippine Sea plate, the FVDs change to nearly NE-SW at 160–320-km depths. There exists an obvious slab gap at the Japan and Izu-Bonin slab junction in the upper mantle and MTZ, and the FVDs along the Izu-Bonin arc and the slab gap exhibit an anticlockwise toroidal trend at 240–640-km depths, which probably reflects corner flow in the mantle wedge due to the tearing and dehydration of the subducting Pacific slab beneath the Izu-Bonin arc. Although the FVDs in the subducting Philippine Sea slab are less well determined as those in the subducting Pacific slab, they exhibit mainly a trench-parallel trend, which is consistent with the spreading direction of the west Philippine basin during its initial opening stage and may reflect frozen-in LPO of aligned anisotropic minerals formed at the mid-ocean ridge and SPO such as normal faults produced at the outer-rise area near the trench axis (e.g., Liu & Zhao, 2017).

### 3.4. Restoring Resolution Tests

We also conducted restoring resolution tests (RRTs; Zhao et al., 1992; Wang & Zhao, 2008) to further evaluate the reliability and robustness of the dominant features in the obtained 3-D  $V_p$  isotropic and anisotropic model. The input model of the RRT is constructed based on the obtained tomographic results, which includes the pattern of  $V_p$  anisotropy, that is, the subduction-parallel FVDs in the upper mantle and subduction-normal FVDs in the MTZ and uppermost lower mantle under the Pacific slab beneath the



Japan arc, the anticlockwise toroidal FVDs beneath the Izu-Bonin arc and the Philippine Sea plate, and the significant isotropic  $V_p$  features, that is, the subducting Pacific slab and hot upwelling flows in the mantle wedge. To perform the RRTs, we adopted the same calculation method for the synthetic traveltimes and the same inversion scheme as those for the CRTs.

Three synthetic tests are performed in this study. In the first synthetic test (Figure S5), we used the synthetic  $P$  wave data generated for the obtained isotropic  $V_p$  anomalies and azimuthal anisotropy in the input model to invert for both the isotropic  $V_p$  variation and azimuthal anisotropy. The second test (Figure S6) is similar to the first one, but the azimuthal anisotropy perturbations are assumed to be zero in the input model, which is used to invert only for the isotropic  $V_p$  variation. The third test (Figure S7) is also similar to the first one, but the isotropic  $V_p$  perturbations are assumed to be zero in the input model, which is used to invert for both the isotropic  $V_p$  variation and azimuthal anisotropy. In all the three tests, Gaussian noise with a standard deviation of 0.1 s is added to the theoretical arrival times before the tomographic inversion. The RRT results (Figures S5–S7) show that both the isotropic and anisotropic  $V_p$  structures are recovered very well, though there exist slight differences in the amplitude of  $V_p$  anomalies due to the uneven ray coverage or fewer rays passing through those parts. Hence, we believe that the velocity heterogeneity and azimuthal anisotropy can be well recovered with little tradeoff by our data set and tomographic method.

## 4. Discussion

### 4.1. Depth-Varying Azimuthal Anisotropy

The Japan Islands are the best place to study subduction dynamics in the world because of the high level of seismicity and availability of the dense and high-sensitivity seismic networks there (see Zhao, 2015, for a detailed review). Our knowledge of seismic azimuthal anisotropy in the Japan subduction zone first came from the SWS measurements (e.g., Ando et al., 1983; Anglin & Fouch, 2005; Hiramatsu et al., 1997; Huang, Zhao, & Wang, 2011; Long, 2013; Nakajima et al., 2006; Okada et al., 1995; Savage et al., 2016; Tono et al., 2009; Wirth & Long, 2010). These SWS results show that the FVD is generally trench parallel in the fore-arc area, while it turns abruptly to be trench-normal in the back-arc area. However, this SWS technique lacks depth resolution and so it is very difficult for us to distinguish the fine anisotropic structures in the crust, mantle wedge, and subducting Pacific slab beneath the Japan arc. The anisotropic tomography methods (e.g., Wang & Zhao, 2008, 2013; Liu & Zhao, 2016a; Liu & Zhao, 2017) can overcome the shortcoming of the SWS method, and many researchers have used the tomographic methods to investigate the 3-D  $V_p$  azimuthal anisotropic structure of the Japan subduction zone in the past decade (e.g., Ishise & Oda, 2005; Wang & Zhao, 2008, 2013; Wei et al., 2015; Huang, Zhao, & Liu, 2015; Liu & Zhao, 2016a; Liu & Zhao, 2017; Niu et al., 2016). Most of these results show that the subducting Pacific slab exhibits mainly trench-parallel FVDs beneath the Japan arc, whereas both the mantle wedge and subslab mantle exhibit trench-normal FVDs. Although these previous studies have improved our understanding of seismic anisotropy, structural heterogeneity, 3-D mantle flow pattern, and subduction dynamics of the Japan subduction zone, they are generally limited to the shallow mantle (<400-km depth), and so deep mantle anisotropic features and their tectonic implications still remain poorly constrained, especially for the subslab mantle at depths of 200–800 km and the stagnant slab in the MTZ. Our high-resolution results reveal the fine-scale isotropic and anisotropic structures of the entire Japan subduction zone down to 1,000-km depth (Figure 6). Because many features of our results are consistent with those of the above mentioned previous results, in the following we mainly discuss and interpret the new features revealed by the present work.

Our results (Figures 6 and 7) show significant FVD variations in the low- $V$  subslab mantle beneath the Japan arc, from the subduction-parallel trend at depths of 160–400 km (Figures 6d–6g) to the subduction-normal trend in the MTZ and uppermost lower mantle (Figure 7). The subslab low- $V$  anomalies exhibit a sheet-like zone subparallel to the Pacific slab at depths of ~100–900 km (e.g., Huang & Zhao, 2006; Wei et al., 2012, 2015). Recent numerical simulations suggest that significant volumes of oceanic asthenosphere materials can recycle back into the deep mantle along with the subducting slab, and even reach as deep as the lower mantle (Liu & Zhou, 2015), a prominent feature consistent with our tomographic results (Figures 6 and 7a–7c). However, the detailed anisotropic features of the subslab mantle under subduction zones remain to be a controversial issue. The SWS measurements show roughly trench-parallel splitting directions existing in the subslab mantle beneath the Japan Trench (e.g., Lynner & Long, 2014a, 2014b; Tono et al., 2009),

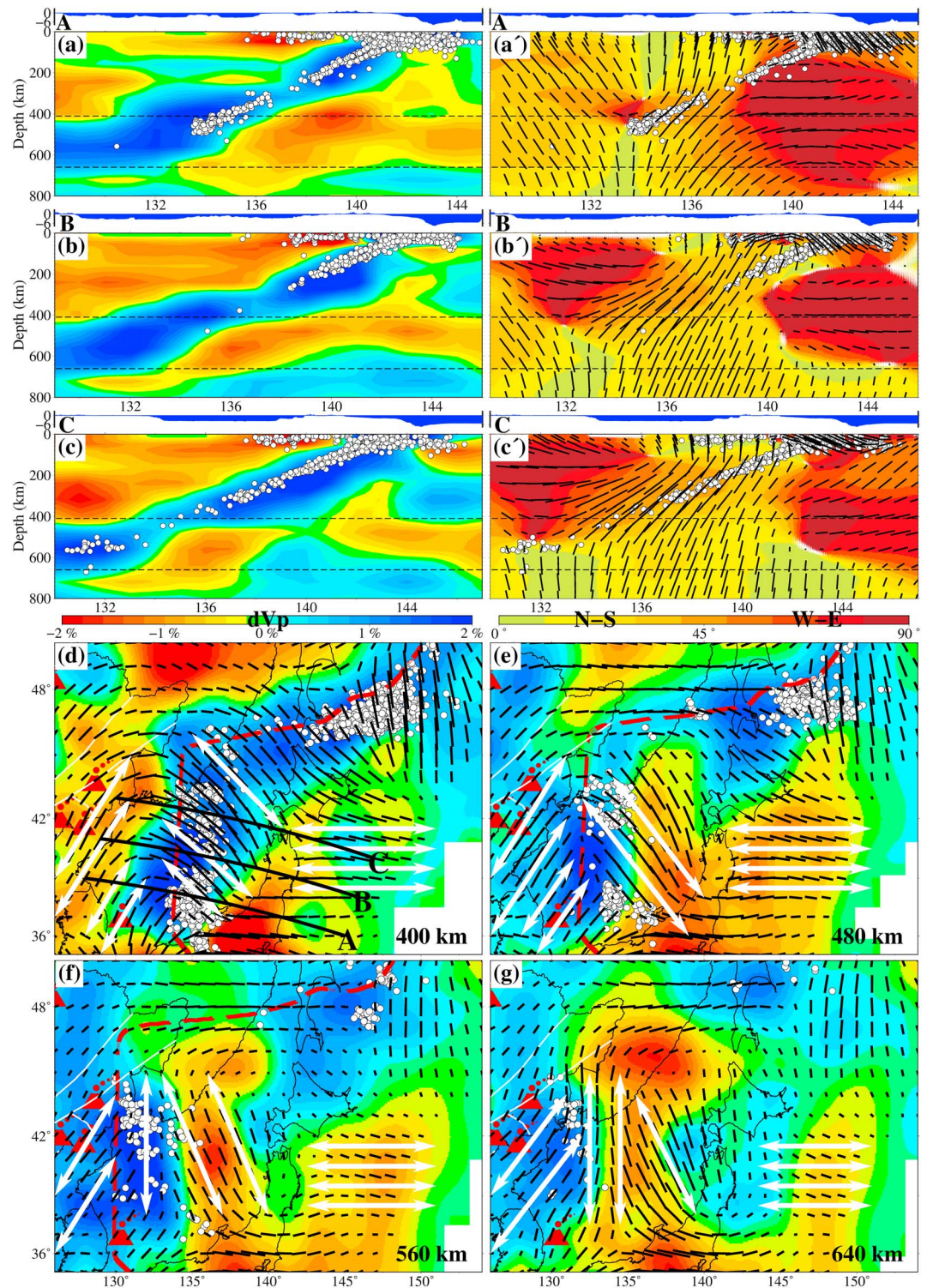


**Figure 7.** (a–c) Vertical cross sections of isotropic  $V_p$  images along three profiles (black lines) shown in (d). (a'–c') Vertical cross sections showing the distribution of  $P$  wave FVDs along the three profiles shown in (d). The surface topography is shown above each cross section. The scales for the isotropic  $V_p$  perturbation (in %) and FVD are shown below the cross sections. The orientation and length of the short black lines denote the azimuth and amplitude of the FVD, that is, vertical lines denote the N-S FVD, whereas horizontal lines denote the E-W FVD. The two dashed lines represent the 410- and 660-km discontinuities. White dots denote the seismicity that occurred within a 40-km width of each profile. (d–g) Map views of  $V_p$  isotropic and azimuthal anisotropy images in and around Japan at depths of 400, 480, 560, and 640 km. The white double arrows denote the dominant FVDs in different areas. The other labeling is the same as that in Figure 6.



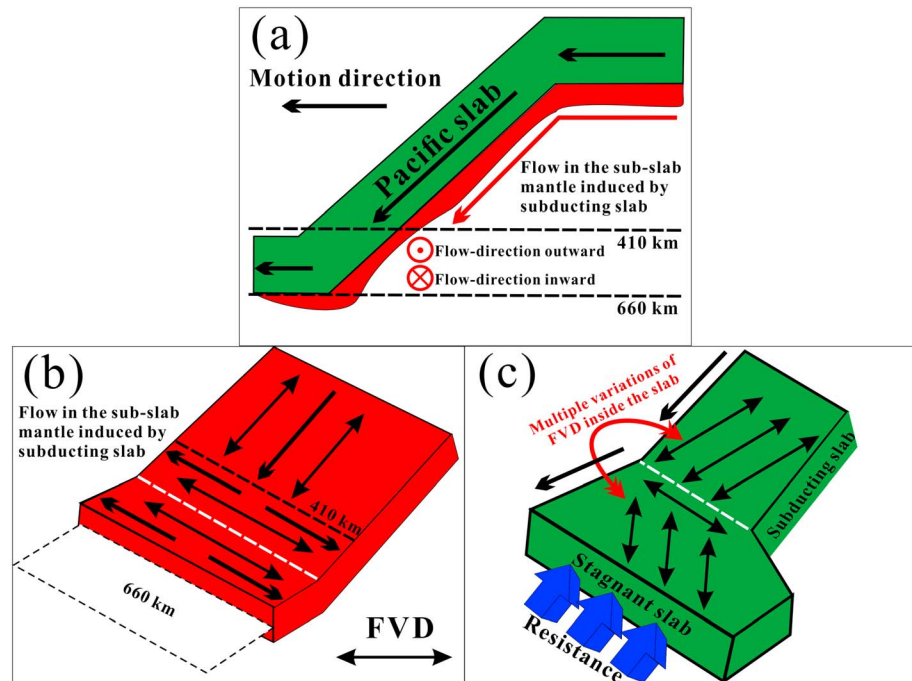


**Figure 8.** Schematic illustrations of (a) an across-arc vertical cross section of the subducting Pacific slab under Japan, (b) dominant FVDs and flow directions in the subslab mantle induced by the subducting Pacific slab, and (c) dominant FVDs inside the subducting Pacific slab.

whereas trench-normal FVDs down to 400-km depth have been revealed clearly by  $V_p$  azimuthal anisotropy tomography (e.g., Wei et al., 2015; see Liu & Zhao, 2016a, for detailed discussions). On the basis of our present results (Figure 6), we propose a qualitative dynamic model (Figures 8a–8b) to interpret the depth-varying seismic anisotropy as shown in Figure 7. The local small-scale anisotropic variations are not considered in our dynamic model due to the limited resolution of our  $V_p$  anisotropic tomography. The subducting Pacific slab entrains a thick layer of subslab mantle material downward to the 410-km discontinuity resulting in entrained 2-D subslab mantle flow, inside which the finite-strain orientations align generally with the plate motion and slab dip caused by the gravitational, pressure or temperature gradients, while A-, C-, or E-type olivine fabrics dominate in the subslab mantle (Lynner & Long, 2014b) to produce the subduction-parallel FVDs in the upper mantle. The MTZ is located between the upper mantle and the lower mantle, where two major seismic discontinuities occur: one at 410 km and the other at 660 km. It is widely believed that the two discontinuities are generally consistent with isochemical phase transitions in the  $(\text{Mg, Fe})_2\text{SiO}_4$  olivine system: olivine to wadsleyite ( $\sim 14$  GPa;  $\sim 410$ -km depth), and ringwoodite to perovskite and ferropericlase ( $\sim 23$  GPa;  $\sim 660$ -km depth; e.g., Ringwood, 1975; Jeanloz & Thompson, 1983; Ito & Takahashi, 1989; Ita & Stixrude, 1992; Christensen, 1995). As shown in Figures 6g–6j and 7, the most significant feature is the FVD variations inside the subslab mantle, with the subduction-parallel FVDs in the upper mantle and the subduction-normal FVDs in the MTZ. The LPO of wadsleyite is regarded as a key factor to cause the MTZ anisotropy because only wadsleyite can produce detectable seismic anisotropy among major minerals in the MTZ (e.g., Karato, 2008; Mainprice, 2007). As the other dominant minerals in the MTZ, ringwoodite and majoritic garnet have only marginal effect on the MTZ seismic anisotropy at the transition zone pressures, because these minerals show elastic anisotropies that are much weaker than that of wadsleyite. Laboratory experiments show that polarization seismic anisotropy observed in the MTZ might be attributed to the preferred orientation of wadsleyite caused by horizontal mantle flow (Kawazoe et al., 2013). Hence, we think that the subslab mantle is sufficiently decoupled from the subducting Pacific slab in the MTZ and uppermost lower mantle to enable approximate 2-D subslab mantle flow directly beneath the slab in the MTZ due to huge resistance resulting from the positive buoyancy effect rendered by mineral phase changes and viscosity jump at the 660-km discontinuity, resulting in predominant subduction-normal FVDs (Figure 8b).



Liu and Zhao (2016b) determined a high-resolution model of *S* wave azimuthal anisotropy tomography of the Japan subduction zone using a large number of high-quality amplitude and phase data of teleseismic fundamental-mode Rayleigh waves at periods of 20–150 s. Their model shows the subducting Pacific slab as a dipping high-*V* zone with significant trench-parallel FVDs. Our present results of *V<sub>p</sub>* azimuthal anisotropy reveal a dramatic FVD variation in the high-*V* subducting Pacific slab beneath Japan, from a trench-parallel trend (NE-SW direction) at depths of 25–80 km (Figures 6a–6c) to an almost trench-normal trend (NW-SE direction) in the lower part of the upper mantle (Figures 6d–6g), whereas visible trench-parallel FVDs are revealed in the hinge part of the stagnant Pacific slab in the MTZ (Figures 6h–6j). The strong trench-parallel FVD in the shallow part of the subducting Pacific slab mainly reflects one or more of the following possibilities: (1) Fossil frozen-in LPO of aligned anisotropic minerals formed at the mid-ocean ridge (e.g., Ishise & Oda, 2005; Liu & Zhao, 2016a; Liu & Zhao, 2017; Tian & Zhao, 2012; Wang & Zhao, 2008, 2013; Wei et al., 2015), (2) SPO in the subducting slab such as normal faults produced at the outer-rise area near the trench axis due to slab bending (e.g., Faccenda et al., 2008; Kobayashi et al., 1998; Masson, 1991), and (3) B-type olivine fabric formed in the old slab through high-stress slab bending in the trench region (e.g., Eberhart-Phillips & Reyners, 2009; Wang & Zhao, 2013). In the deeper portion of the subducting Pacific slab (~160–400-km depths), however, the FVDs are totally different, being trench normal. The SWS measurements (Tono et al., 2009) suggest that the fossil seafloor spreading anisotropy frozen in the Pacific plate can be preserved to depths greater than 400 km inside the subducting slab during its downward journey. However, our present results do not support this suggestion. It has been widely accepted that subducting lithospheric plates undergo metamorphism and deformation as they descend into the mantle, which can result in profound changes in mineralogy, structure, rheology, and fluid content of the subducting slabs. As the slab continuously descends (>100-km depth), most of the water stored in hydrous minerals is progressively removed. Once the slab has dehydrated, further metamorphic reactions and recrystallization will obliterate any dehydration-induced crack damage and the seismic anisotropy in the slab will be dominated by the LPO of anhydrous minerals alone, which can result in the trench-normal FVD in the deep portion of the subducting slab, because the finite strain orientations align generally with the Pacific plate motion and the subducting slab dip under the deep mantle temperatures and pressures. The above mentioned mechanism can well explain the depth-varying azimuthal anisotropy in the subducting Pacific slab (<400-km depth), from the nearly trench-normal FVD to the trench-parallel FVD.

Although it is well known that the Pacific slab becomes horizontal and stagnant in the MTZ beneath East Asia (e.g., Bijwaard et al., 1998; Fukao & Obayashi, 2013; Huang & Zhao, 2006; Li & van der Hilst, 2010; Liu et al., 2017; Ma et al., 2018; Wei et al., 2012, 2015; Zhao, 2004), seismic anisotropy of the stagnant slab in the MTZ is still not well understood. Seismic investigations for azimuthal anisotropy in the MTZ, however, are quite difficult because long-wavelength surface waves have limited spatial sensitivity at the MTZ depths and teleseismic body waves have a very low depth resolution. Thanks to the development of the tomographic method and the large number of high-quality seismic data used in this study, the fine-scale stagnant slab anisotropy in the MTZ has been generally revealed in our present model with an unprecedented lateral and vertical resolution at depths of the MTZ and the uppermost lower mantle (Figures 6 and 7), providing new constraints on the dynamic process of the slab deep subduction beneath East Asia. The Pacific slab has been subducting at a rate of ~9 cm/yr and arrived at the 660-km discontinuity beneath Northeast China. However, because of the huge resistance at the 660-km discontinuity, the subducting slab bends horizontally and becomes stagnant in the MTZ beneath East Asia for no more than ~10–20 million years (Liu et al., 2017). As shown in Figures 6h–6j and 7, the NE-SW FVDs revealed in the hinge part of the stagnant Pacific slab are roughly parallel to the Japan Trench and normal to the slab subduction direction. Although the deformation mechanism inside the stagnant slab in the MTZ remains poorly understood, SS precursor results suggest that the stagnant part of the subducted Pacific plate is not as flat as previously suggested (Gu et al., 2012) with the strong deformations in the center of the stagnant slab. It is believed that trench migration and slab rollback have no significant effect on the deformation process in the stagnant slab, because the entire Pacific slab is under the huge compressive stress regime in the depth range of 100–660 km (e.g., Zhao et al., 2009) and extends >2,000 km westward from the Japan Trench (Figures 10 and 11). Thus, the Pacific slab may not roll back significantly but rather continuously subduct and have moved laterally westward within the upper mantle and MTZ after subduction at near-plate tectonic rates (~2 cm/yr over 50 Ma; Wu et al., 2016). Therefore, we deem that the great resistance from the 660-km discontinuity can

prevent the subducting slab from penetrating into the lower mantle. When the stagnant slab continues to move laterally westward, the substantial resistances in front of the western edge of the flat slab will also play an important role in causing strong deformation inside the stagnant slab in the MTZ. Both of the effects can in turn align mineral aggregates and produce the dominant trench-parallel FVD, which further indicates that dislocation creep may be the dominant deformation mechanism in the MTZ beneath the NW Pacific subduction zone.

#### 4.2. Slab Tearing Under the Izu-Bonin Arc

The Izu-Bonin-Mariana (IBM) arc system lies along the eastern margin of the Philippine Sea plate in the western Pacific Ocean. The IBM arc system formed as a result of multistage subduction of the western Pacific plate beneath the Philippine plate stretches over 2,800 km south from the Tokyo Bay to beyond Guam and consists of the Izu-Bonin arc in the north and the Mariana arc in the south (Figure 1a). The Pacific plate moves northwestward relative to IBM, at a rate varying from ~6 cm/yr in the north to ~2 cm/yr in the south (Seno et al., 1993). Beneath the Mariana arc, it is well understood that the Pacific slab penetrates the 660-km discontinuity into the lower mantle down to a depth of ~1,000 km (e.g., Bijwaard et al., 1998; Fukao & Obayashi, 2013; Gorbatov & Kennett, 2003; Rost et al., 2008; Tibi et al., 2006, 2007; Widiyantoro et al., 1999; Zhao et al., 2017), which shows a roughly 80° dipping slab with a clear Wadati-Benioff deep seismic zone toward the northwest. Under the Japan and Izu-Bonin arcs, Obayashi et al. (2009) revealed a laterally continuous subducting slab along the Kurile, Japan, and Izu-Bonin arcs down to a depth of ~300 km. However, the Japan and Izu-Bonin slab images are disconnected from each other at their junction (~35°N) just below 300-km depth, indicating a slab gap, which is much more clearly revealed by our present high-resolution  $V_p$  anisotropic tomography (Figures 6 and 9). They suggested that the Izu-Bonin and the Japan slabs meet each other to form a cusp-like junction beneath southwest Japan and the two slabs are torn apart at their junction when they bend to flatten over the 660-km discontinuity. Meanwhile, the morphology of the subducting slabs has been delineated by the analysis of depth distribution of seismicity in the Wadati-Benioff zone and several different regional-scale tomographic studies. The Pacific slab across the Japan arc, Japan Sea, and East Asian continent shows a continuous high-V structure deflected horizontally within or just beneath the MTZ, and intermediate-depth and deep earthquakes occurred actively in the subducting slab with a dip angle of ~30°; farther south beneath the Izu-Bonin arc, the slab becomes much steeper with a dip angle of 50°–70° in the upper mantle and flats in a nearly subhorizontal fashion in the MTZ or penetrates into the lower mantle (e.g., Huang & Zhao, 2006; Li & van der Hilst, 2010; Miller et al., 2006; Wei et al., 2012, 2015; Zhao et al., 2017).

Our  $V_p$  anisotropic tomography has a very good resolution in the NW Pacific subduction zone and shows an obvious gap inside the subducting Pacific slab beneath southern Honshu that can be tracked from the shallow upper mantle to the MTZ (Figures 9b–9f), which has been described from analysis of distinct  $P$  to  $S$  converted phases at the edge of the zone and tensional focal mechanisms of deep earthquakes in the tear zone (e.g., Kennett & Furumura, 2010; Obayashi et al., 2009). The agreement in the gap-like structure among the different studies indicates that it is a well-resolved feature rather than an artifact of tomographic inversion. It should be noted that large-scale low-V anomalies with NE-SW FVDs are visible within the upper mantle and the MTZ beneath the Philippine Sea plate, which seem to originate from the mantle flows in the Pacific subslab mantle through the gap between the Izu-Bonin slab and the Japan slab (Figures 6 and 9a–9f). In addition, as the depth increases, the slab tear becomes wider, while the scale and amplitude of the low-V anomalies under the Philippine Sea plate become smaller and weaker. Beneath the southern part of the Izu-Bonin arc, the Pacific slab penetrates into the lower mantle with strong deformation in the MTZ and uppermost lower mantle (Figure 9g), suggesting that the penetrated slab meets strong resistance at the 660-km discontinuity. As discussed above, Obayashi et al. (2009) roughly attributed the Pacific slab tear and consequent slab gap to the slab stagnation in the MTZ and seem to ignore the great differences in the subduction rate, direction, and dip of the different slabs between two adjacent segments. We think that the joint effect of the above mentioned key factors may be the main cause of the Pacific slab tear at the Japan and Izu-Bonin slabs junction. When the Japan slab bends to flatten in the MTZ and the southern Izu-Bonin slab directly penetrates into the lower mantle, the consequent slab gap will continue to extend and further trigger complex 3-D mantle flow field around the gap.

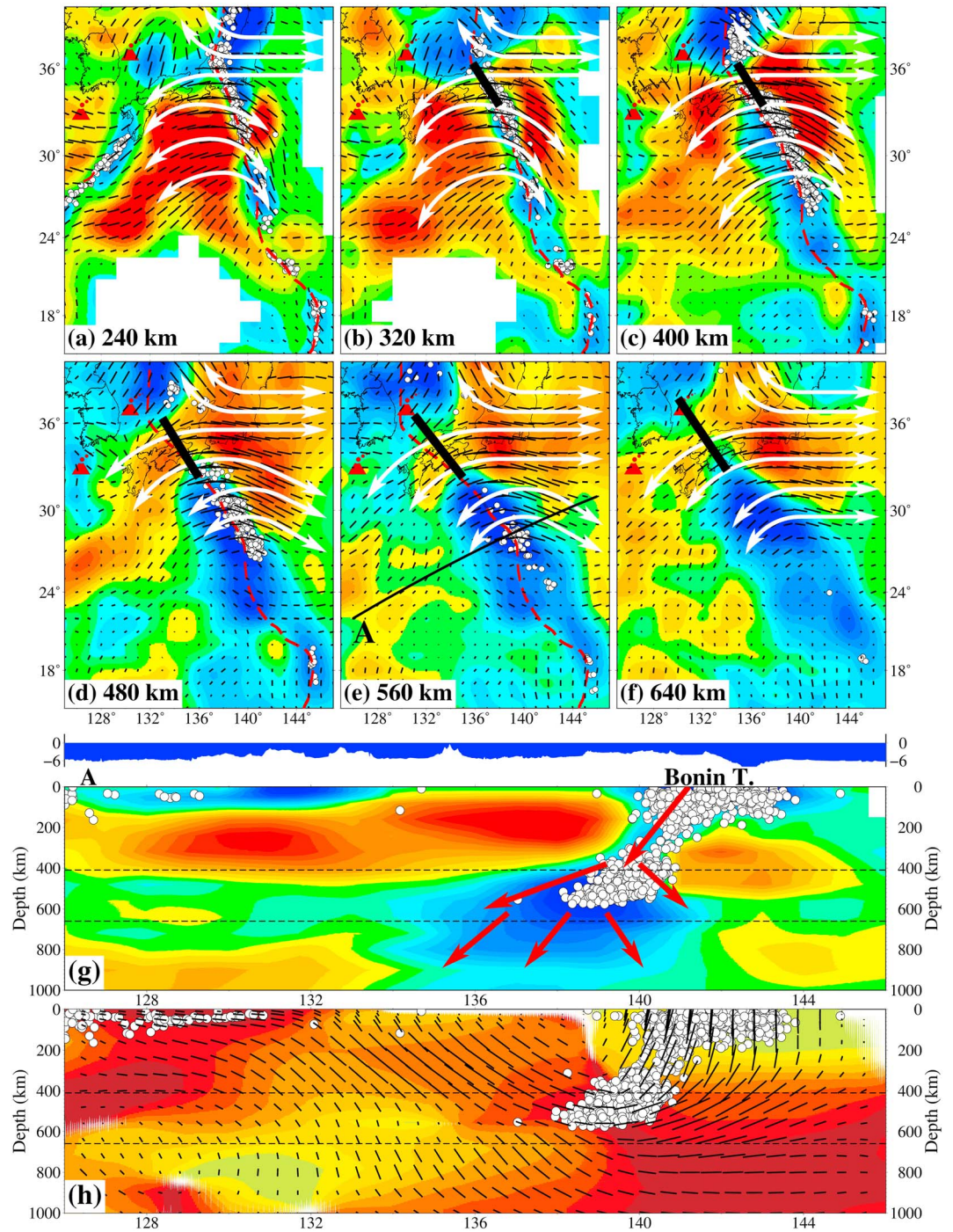


**Figure 9.** (a–f) Map views of  $V_p$  isotropic and azimuthal anisotropy images in and around the Izu-Bonin arc at the depth shown in each map. The white double arrows denote the dominant FVDs and toroidal mantle flow around the slab gap marked with the thick black bar. The other labeling is the same as that in Figure 6. (g and h) Vertical cross sections of  $V_p$  anisotropic tomography and FVDs along the profile (black line) shown in (e). The other labeling is the same as that in Figure 7.

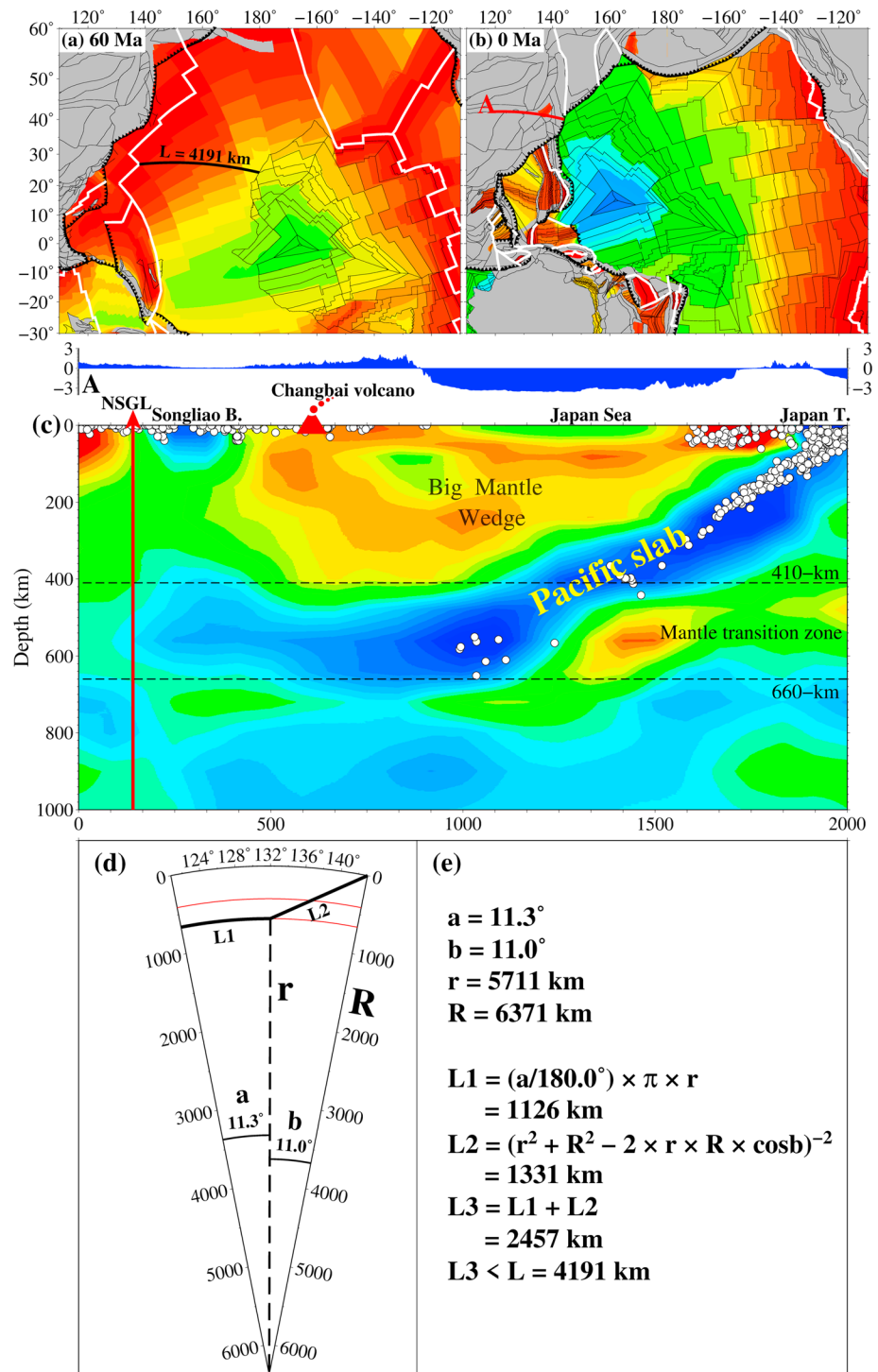
As a characteristic feature of the Earth's interior medium, seismic anisotropy, produced primarily due to the LPO of olivine in the upper mantle, has often been used to study mantle deformation and the geometry of mantle flow in tectonically active regions, such as subduction zones, where slab dehydration and fluid-triggered melting are very important processes. The FVDs along the Izu-Bonin arc and the tearing gap



exhibit a striking anticlockwise toroidal trend at 240–640-km depths (Figures 9a–9f), suggesting that the occurrence of the slab tearing may have caused a complex flow pattern in the mantle wedge above the Pacific slab and the Pacific subslab mantle beneath the Izu-Bonin arc. Many numerical simulations have suggested that the toroidal mantle flow pattern could be driven around the subducting slab edge due to slab rollback or complexity in slab shape (e.g., Faccenda & Capitanio, 2012, 2013; Jadamec & Billen, 2010; Piromallo et al., 2006; Stegman et al., 2006). Meanwhile, the toroidal mantle flow pattern is consistent with many seismic anisotropy observations in the subduction zones (e.g., Castellanos et al., 2018; Civello & Margheriti, 2004; Liu & Zhao, 2016a; Paul et al., 2014; Wei et al., 2016; Zandt & Humphreys, 2008). However, these mechanisms seem not to well explain our present anisotropic results, where the slab tearing may play an important role. The recent 3-D geodynamic modeling results also show that the development of a tear in the subducting slab has a significant influence on the fast polarization direction due to stronger mantle flow through the slab window, and a circular pattern around the slab edges can be produced (Confal et al., 2018). As discussed in section 4.1, the subducting Pacific slab can entrain the thick and sheet-like subslab mantle materials down to the MTZ and uppermost lower mantle, which can cause huge pressure, temperature, or gravitational gradients between the mantle wedge above the Pacific slab and the subslab mantle. Therefore, we think that part of the subslab mantle flow may be sufficiently decoupled from the overlying subducting Pacific slab because of the occurrence of the slab-tearing process, and in such a case, the great differences in the pressure gradient can drive the subslab mantle flow like squeezing toothpaste from a tube, upward into the mantle wedge through the slab gap. The anticlockwise toroidal mantle flow in and around the Izu-Bonin trench and the gap was caused by joint effects of several factors, including the much steeper Izu-Bonin slab than the Japan slab, different rheological properties of the two mantle wedges, and complex interactions among the different convective circulation processes in the mantle wedge and the ambient mantle. These 3-D mantle flow patterns can better explain the large variations of  $V_p$  azimuthal anisotropy in the Izu-Bonin subduction zone. Our understanding of the geometry and composition of the subducting Pacific slab and the physical process of subduction mostly comes from indirect observations including seismology (e.g., earthquake hypocenters, seismic structure, anisotropy, and attenuation), gravity, geochemistry, and petrology of Island arc lavas. Recent advances in high-resolution geodynamic modeling will allow us to test the hypothesis, which can be achieved via the adjoint method and retrodictions of the past mantle flow that assimilate seismic images of the mantle (e.g., Bunge et al., 2003; Colli et al., 2018).

### 4.3. Intraplate Volcanism and Mantle Dynamics

The Pacific-Izanagi spreading ridge began to subduct under the East Asian margin between 55 and 50 Ma and further replaced by the western Pacific Plate, which continued to move westward and subduct in the northwestern direction (e.g., Müller, Sdrolias, Gaina, Steinberger, & Heine, 2008; Seton et al., 2015). It is well known that the Izanagi plate has completely penetrated into the lower mantle and a large amount of slabs now founder at the core-mantle boundary (e.g., Amaru, 2007; Li et al., 2008; Obayashi et al., 2013; Seton et al., 2015; Simmons et al., 2012; Zhao, 2004). As mentioned above, many seismic observations have consistently shown that the subducted slab is deflected horizontally for a long distance (>1,000 km) in the MTZ beneath East Asia, which is often attributed to the subducting Pacific plate initiating in the Paleocene. The reconstruction of global plates and numerical modeling of oceanic basin dynamics (Müller et al., 2016) suggest that at least 4,100 km of the Pacific slab has been absorbed by the western Pacific subduction zone since the onset of the Pacific plate subduction beneath East Asia at ca. 55 Ma (Figures 10a and 10b). Figure 10c shows a vertical cross section along the great circle, which passes through the Changbai intraplate volcano and the northeast Japan arc. A rough estimation (Figures 10d and 10e) shows that the length of the imaged subducting slab in the upper mantle and MTZ under Northeast Asia is only ~2,400 km, which is about a half of the extinct slab. This result suggests that the subducting Pacific slab may have suffered significant oceanic lithospheric shortening and the flat slab now in the MTZ beneath East Asia is the subducted Pacific slab rather than the Izanagi slab (e.g., Liu et al., 2017). Recent global mantle convection models show that a thin and weak layer at 670-km depth from spinel to postspinel phases plays an important role in producing slab stagnation in the MTZ, and the stagnant slab under East Asia largely results from subduction in the past 20–30 Myr, suggesting a transient nature of slab stagnation on a timescale of tens of millions of years (Mao & Zhong, 2018).



**Figure 10.** The seafloor age distribution in the western Pacific at (a) 60 and (b) 0 Ma (modified from Müller et al., 2016). The other labeling is the same as that in Figure 1b. (c) An east-west vertical cross section of isotropic  $V_p$  tomography along the profile (red line) shown in (b). The vertical red single arrow indicates the location of the NSGL in eastern China. The other labeling is the same as that in Figure 7. (d) A schematic diagram showing the procedure of estimating the length of the present subducting Pacific slab along the profile (red line) shown in (b). The values of the parameters used in the estimation are shown in (e).



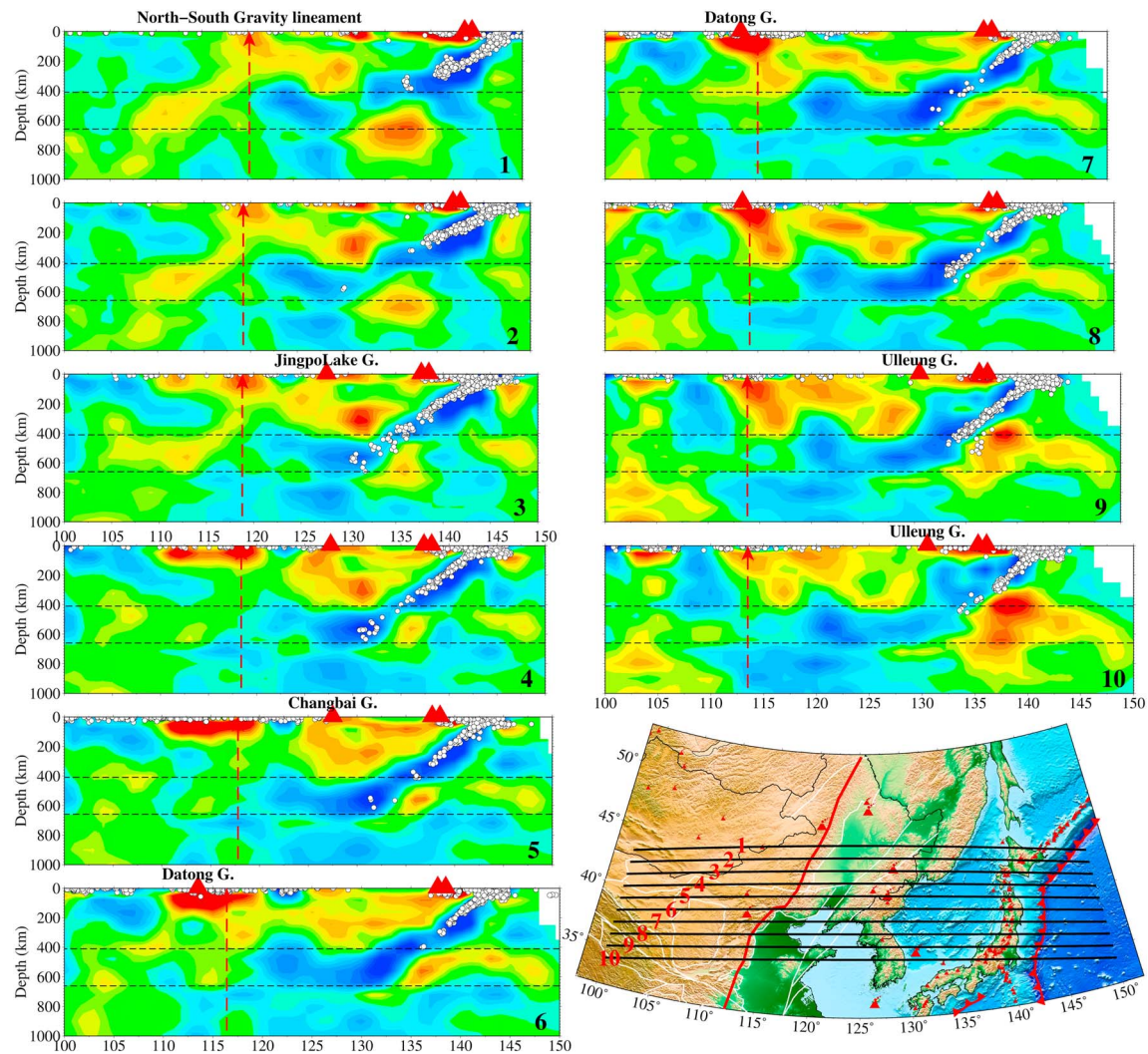


**Figure 11.** (1–10) Vertical cross sections of isotropic  $V_p$  tomography along the ten profiles (black lines) shown on the inset map. The red dashed lines denote the location of the NSGL, and the red triangles denote active volcanoes. The other labeling is the same as that in Figure 7.

It is considered that the stagnant Pacific slab in the MTZ has contributed to the widespread Cenozoic magmatism and intraplate volcanism in northeast China and surrounding regions (Figure 11; e.g., Lei & Zhao, 2005; Huang & Zhao, 2006; Zhao et al., 2009; Wei et al., 2012, 2015; Tian et al., 2016; Chen et al., 2017; Ma et al., 2018). The broad upper mantle region above the stagnant Pacific slab has formed a big mantle wedge (BMW) beneath East Asia (e.g., Liu et al., 2017; Zhao, 2004; Zhao et al., 2009). The subduction-driven corner flow in the BMW and fluids from deep dehydration reactions of the stagnant slab and/or fluids brought down from the shallow mantle wedge by convective circulation process are considered to be responsible for the extensive Late Mesozoic–Cenozoic tectonomagmatism, significant intraplate volcanoes, intraplate earthquakes, continental lithosphere destruction, and the west-east boundary in the surface topography and gravity anomaly in East Asia (Figures 10c, 11, 12, 15b, and 15c). This BMW model has been supported by most of the multiscale tomographic studies, and many geophysical, geochemical, and numerical simulation results (see recent reviews by Zhao & Tian, 2013; Xu et al., 2018, and Zhang et al., 2018). However, Tang et al. (2014) and Tao et al. (2018) show the existence of a very narrow low- $V$  anomaly within the stagnant slab beneath northeast China, interpreted as a slab gap, through which a thin low- $V$  zone from the top of the lower mantle up to the surface finally feeds the Changbai volcanism. But this feature is not visible in other recent tomographic models of East Asia (e.g., Chen, Zhao, et al., 2017; Ma et al., 2018; Takeuchi et al., 2014; Wei et al., 2015). Thus, the origin of the Changbai volcano remains to be a controversial issue. Our present

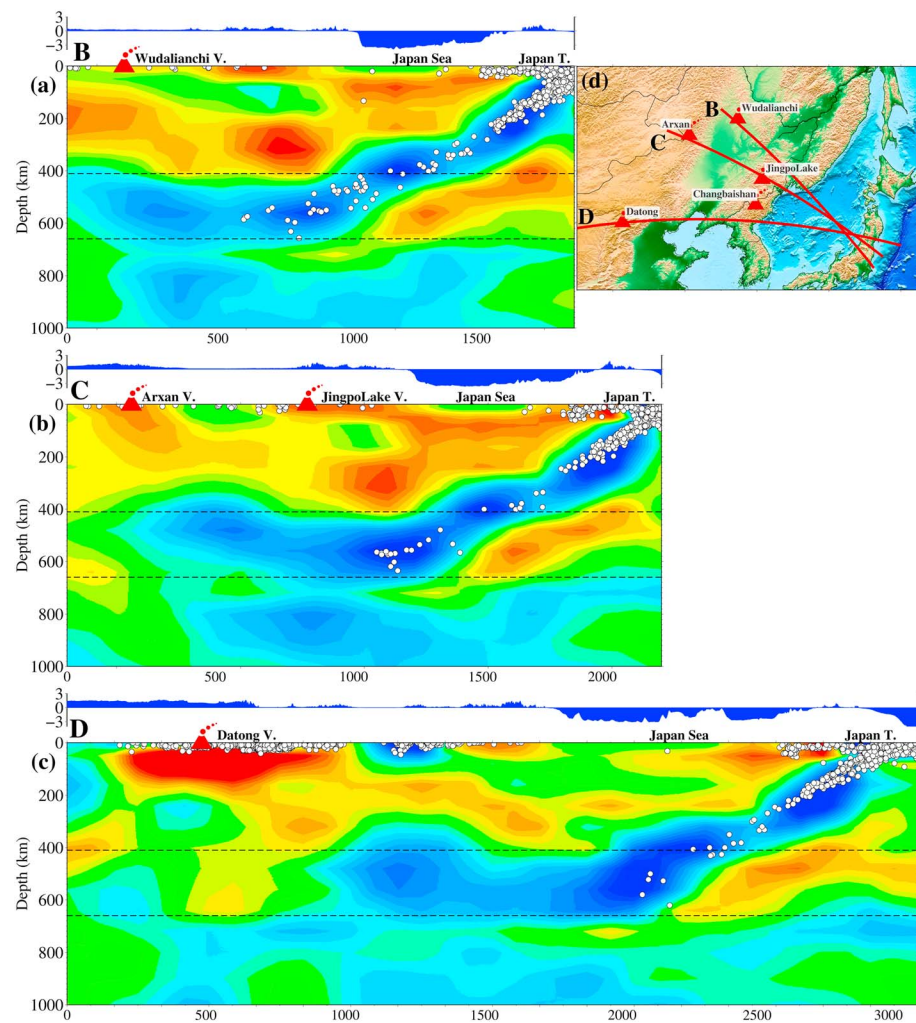


**Figure 12.** (a–c) Vertical cross sections of isotropic  $V_p$  tomography along the three profiles (red lines) shown on the inset map (d). The other labeling is the same as that in Figure 7. See the text for details.

results of  $V_p$  isotropic and azimuthal anisotropy tomography (Figures 6h–6j), derived from absolute traveltimes residuals, show a continuous Pacific slab without the so-called slab gap. The slab is deflected horizontally in the MTZ under East China, and the western edge of the stagnant slab is well coincident with the surface topographic boundary and the NSGL in East China (Figures 15b and 15c). The toroidal FVDs down to 320-km depth (Figures 6a–6f) are roughly revealed in and around the Jingpo, Changbai, and Longgang volcanic groups in the southeastern margin of the Songliao Basin. This result provides direct observational evidence for the interaction between the overlying cold lithosphere and the hot and wet mantle upwelling caused by joint effects of deep slab dehydration and convective circulation process in the BMW beneath Northeast Asia.

The Wudalianchi volcano is one of the youngest volcanoes in the Asian continent, which formed during five eruptive cycles from the early Pleistocene to historical time with its recent eruption in 1719–1721. Similar to the Changbai volcano, significant low- $V$  anomalies in the upper mantle and a horizontal high- $V$  zone in the MTZ are also detected beneath the Wudalianchi (Figure 12a), Arxan and Jingpo volcanoes (Figure 12b), implying the same formation mechanism of the three intraplate volcanoes as the Changbai volcano (e.g., Wei et al., 2019). These results indicate that the Cenozoic intraplate volcanoes in NE Asia are not hot spots related to deep mantle plumes but caused by the BMW processes associated with the deep subduction of the western Pacific plate (Figures 14 and 15a; e.g., Zhao, 2004; Lei & Zhao, 2005; Huang & Zhao, 2006; Wei et al., 2012, 2015; Zhao & Tian, 2013; Chen, Zhao, et al., 2017; Ma et al., 2018).



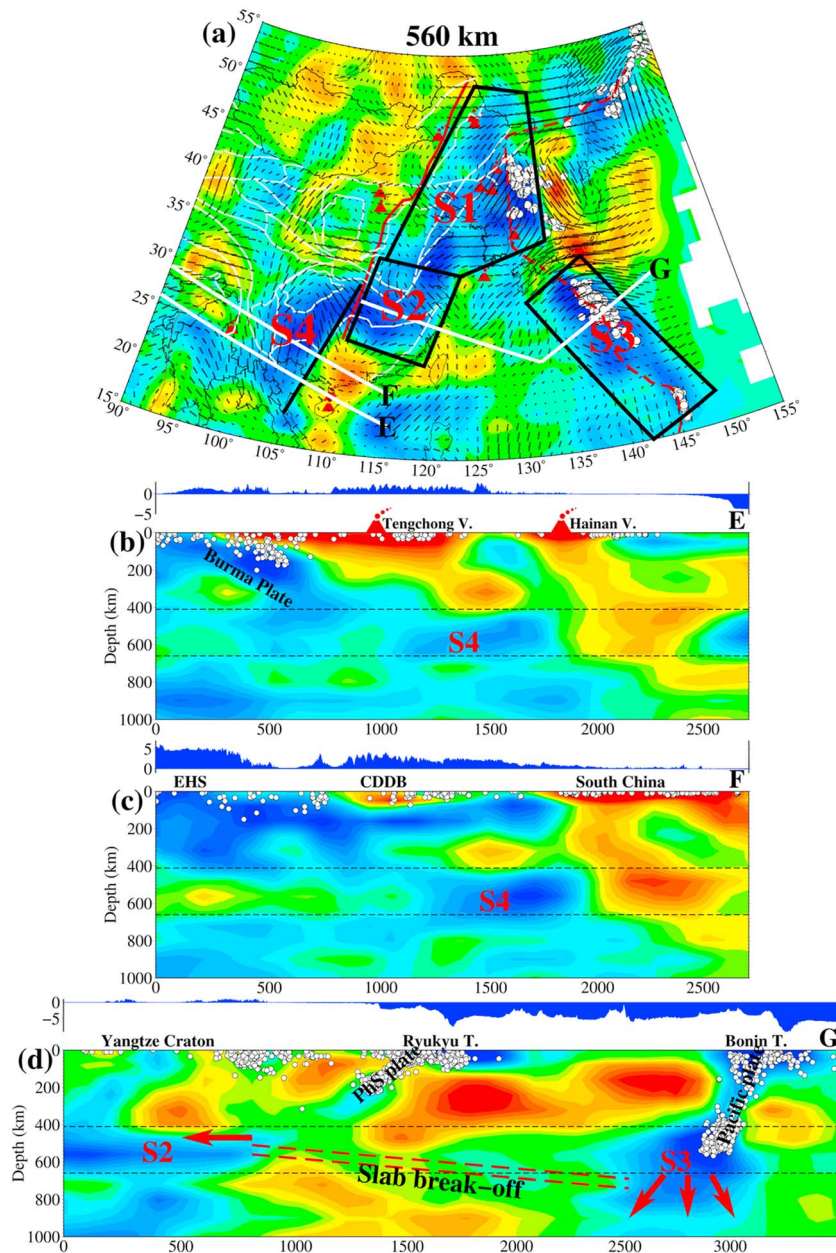


**Figure 13.** (a) Map view of  $V_p$  isotropic and azimuthal anisotropy image at 560-km depth. The anomalous features S1, S2, S3, and S4 are discussed in the text. The black boxes show the limits of S1, S2, and S3. The eastern edge of S4 is marked by a black line. (b–d) Vertical cross sections of isotropic  $V_p$  tomography along the three profiles (white lines) shown in (a). CDDB, the Chuandian Diamond Block; EHS, the Eastern Himalayan Syntax. The other labeling is the same as that in Figure 7. See the text for details.

The Quaternary Datong volcano is located in the northern portion of the Shanxi rift, which is about 2,500 km away from the Japan Trench (Figure 1a). The origin of the Datong volcano has been the target of many tomographic studies (e.g., Huang & Zhao, 2006; Lei, 2012; Tao et al., 2018; Tian et al., 2009). However, the origin of the Datong volcano remains unclear due to the lack of higher-resolution tomographic models. Our present model (Figure 12c) shows an obvious low- $V$  anomaly in the upper mantle under the Datong volcano, which is connected with the low- $V$  zone in the BMW. The low- $V$  anomaly under Datong extends to the MTZ bottom but not to the lower mantle, which is consistent with previous tomographic results. We speculate that the MTZ low- $V$  anomaly in front of the western edge of the stagnant slab may reflect an upwelling flow triggered by the westward push of the stagnant slab, which may have caused the Datong volcanism.

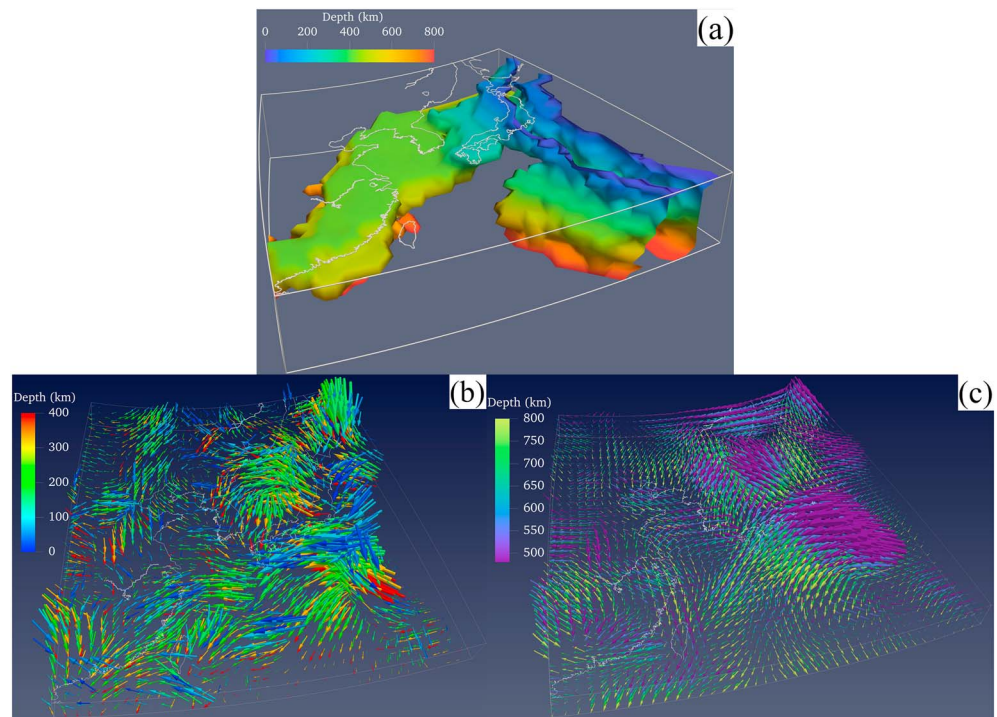


**Figure 14.** (a) A 3-D view of the subducting Pacific slab (with  $V_p$  perturbations  $\geq 0.5\%$ ) under East Asia. 3-D views of the FVDs in the upper mantle (b) and the MTZ and the uppermost lower mantle (c).

At depths of 480–1,000 km, broad high- $V$  anomalies are visible under East China, which are consistent with previous  $P$  wave tomography models (e.g., Huang & Zhao, 2006; Li & van der Hilst, 2010; Obayashi et al., 2013; Tao et al., 2018; Wei et al., 2012, 2015) but show more structural details in the MTZ and lower mantle because of the more uniform and denser ray coverage in our data set. The tomographic image at 560-km depth (Figure 13a) shows that several separated high- $V$  anomalies exist in the MTZ: S1 is a NNE striking structure beneath north and northeast China, the Bohai Sea, the Yellow Sea, and the Japan Sea; S2 is a NNE striking structure beneath the Yangtze Craton and the south China fold system, both of which are parallel to the Japan Trench and located in the east of the NSGL; S3 is a NNW striking structure beneath the Izu-Bonin and Mariana arcs; and S4 is a NE striking structure beneath the western part of the Yangtze Craton.

After decades of regional and global tomographic studies, it is undoubted that S1 can be interpreted as fragments of the subducting Pacific slab, produced by subduction of the Pacific plate beneath the Eurasian plate along the Japan Trench, as discussed above. The NE striking structure S4 is roughly located in  $20^\circ$ – $32^\circ$ N and  $100^\circ$ – $110^\circ$ E, at depths of 450–700 km (Figures 13b and 13c), and its orientation and position suggest that it is difficult to be produced by multiperiod subduction of the Pacific plate or the Philippine Sea plate (e.g., Müller et al., 2016). S4 is similarly observed by previous studies: Li and van der Hilst (2010) interpreted it as a slab that subducted 60–80 Ma along the southeastern coast of China, whereas Tao et al. (2018) speculated it to be related to the subduction of the *proto-South China Sea* at 20–30 Ma (Wu et al., 2016). However, the cross sections through S4 (Figures 13b and 13c) show an ESE striking subduction direction in the upper mantle beneath the Chuandian Diamond Block and the Eastern Himalayan Syntax, and S4, as a stagnant high- $V$  anomaly in the MTZ, is not connected to the mantle structures under the South China Sea or the southeast of the South China Fold system but closely related to the recent subduction of the Burma microplate and/or Indian plate beneath Southeast Asia. Above the high- $V$  zone (S4), a prominent and rather broad low- $V$  zone is visible from the top of the MTZ up to the surface beneath the active Tengchong volcano in SW China. Our results indicate that the origin of the Tengchong volcano is closely related to the eastward deep subduction of the Burma microplate (or the Indian plate), which is similar to the formation mechanism of the Changbai volcano in northeast China as discussed above. Geochemical and multiscale tomographic studies suggest the presence of the Hainan mantle plume (e.g., Ho et al., 2000; Lebedev & Nolet, 2003; Wei et al., 2012; Xia et al., 2016; Zhao, 2004). Our present tomographic model



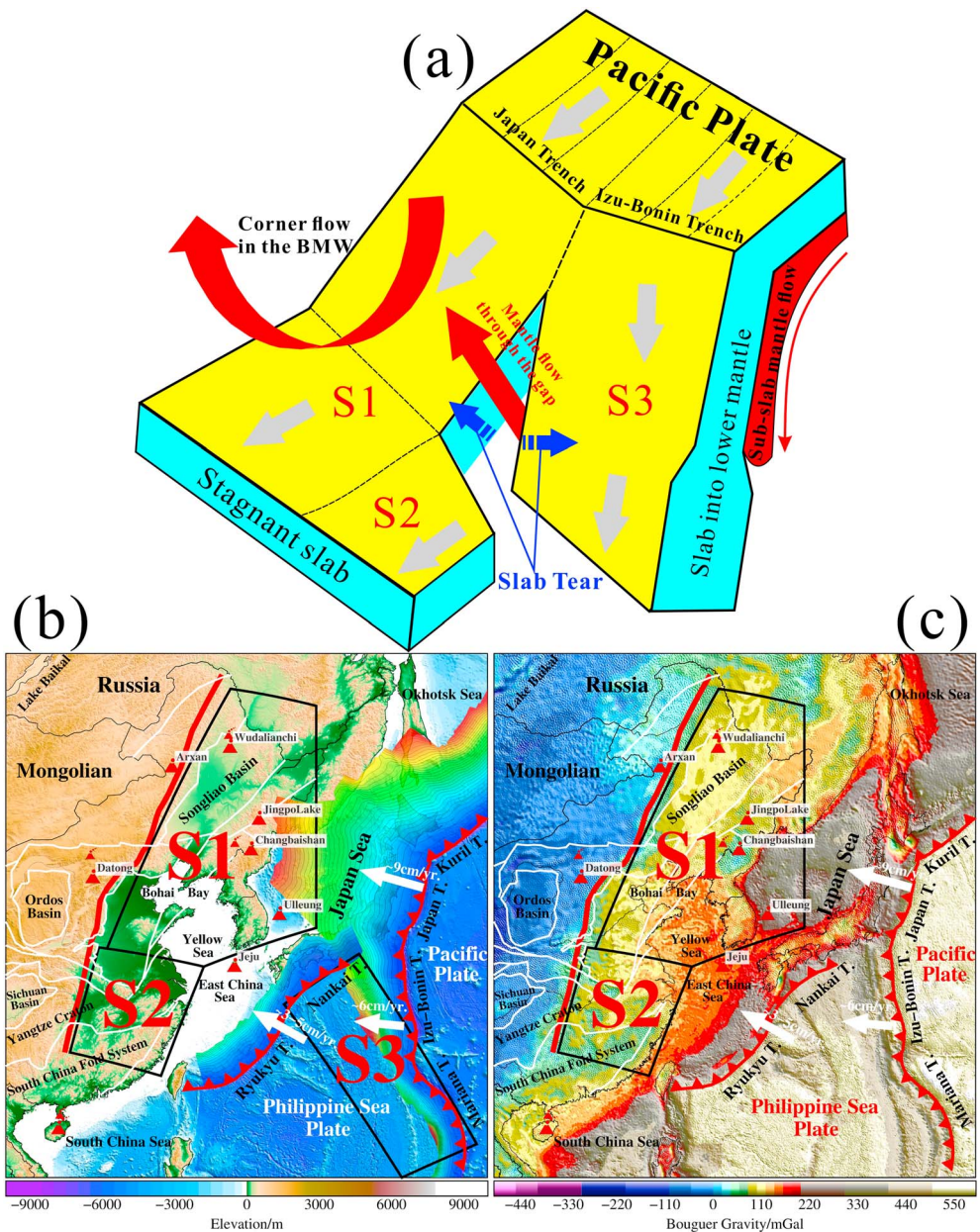


**Figure 15.** (a) A schematic diagram illustrating main features of the subducting Pacific slab beneath Western Pacific and East Asia, including corner flow in the big mantle wedge (BMW), subslab mantle flow, and flow through the slab gap between the Japan and Izu-Bonin trenches. (b) Surface topography and (c) Bouguer gravity anomalies (derived from Balmino et al., 2012) in the study region. The other labels are the same as those in Figures 1a and 12.

shows that the Hainan Island and southeast China are underlain by a plume-like low-V zone extending down to ~900-km depth, but our current model cannot provide more detailed features of the Hainan plume in the lower mantle.

There is no dispute for S3 that can be interpreted as the subducting Pacific slab beneath the Philippine Sea plate along the Izu-Bonin and Mariana trenches. But there are still different opinions about S2. Tao et al. (2018) suggest that S2 may be the detached Philippine Sea slab beneath East China, based on their tomographic results and plate reconstructions. However, our present results do not support their suggestion. Although ~625-km length of the Philippine Sea plate has subducted down to 450-km depth as they imaged, it is still very short compared with the subduction scale of the western Pacific plate, as mentioned above. The position of S2 far west of the Ryukyu Trench further indicates that S2 was not produced by the subducting

Philippine Sea plate, but the subducting Pacific slab beneath the Izu-Bonin Trench (e.g., Huang & Zhao, 2006; Li & van der Hilst, 2010; Wei et al., 2012). Therefore, we think that the high-V anomalies (S1 and S2) in the MTZ under east China are actually the same stagnant Pacific slab rather than several segmented structures (Figure 14a). Our result (Figure 13d) shows that a slab break off may exist between the southern part of S2 and the subducting Pacific slab beneath the Bonin arc, considering that the Izu-Bonin and the Japan slabs are torn apart below ~300-km depth at their junction and the Bonin slab has penetrated the 660-km discontinuity and reached the lower mantle. This is quite speculative, but it may explain the enigmatic phenomenon that the subhorizontal north-south extent of the stagnant Pacific slab in the MTZ under east China is far greater than that of the Japan Trench.

It has been long debated whether part of the subducting Pacific slab material has sunk into the lower mantle under east China. Our present tomographic images show that large-scale NE striking high-V anomalies in the uppermost lower mantle continuously exist down to 1,000-km depth or even deeper in the east of the NSGL, which may represent fragments of the Pacific slab and/or ancient continental lithosphere collapsing down to the lower mantle. The NSGL, as an important tectonic line in Mainland China, exhibits sharp variations in the surface topography, gravity anomaly, crustal and lithospheric thickness, and mantle seismic velocity from the east to the west (e.g., Xu, 2007). In Figures 15b and 15c, we compare the surface topography and Bouguer gravity anomalies in east China and adjacent regions with the extent of the stagnant Pacific slab at 560-km depth. The western edge of the Pacific stagnant slab is well coincident with the surface topographic boundary along the NSGL in east China. The subduction and stagnancy of the Pacific plate under the Eurasian continent may have a profound influence on the evolution of the surface tectonics and gravity anomaly, and structure and dynamic processes in the BMW (Figures 11, 14, and 15a; Huang & Zhao, 2006; Zhao & Tian, 2013), but the current tomographic results cannot provide further constraints on the detailed formation mechanism. Future higher-resolution seismological studies and geodynamic modeling may be able to shed new light on this interesting phenomenon (e.g., Colli et al., 2018; Fichtner et al., 2018; Wei et al., 2019).

## 5. Conclusions

To better understand the detailed 3-D anisotropic structure and dynamics of the western Pacific and East Asian region, we determine high-resolution *P* wave azimuthal anisotropy tomography down to 1,000-km depth using ~1.87 million high-quality *P* wave arrival times from 84,777 local and regional earthquakes recorded at ~3,000 seismic stations compiled by the China National Seismic Network, the Japanese Kiban Seismic Network, and the International Seismological Center. Our results provide new insights into the anisotropic structure and subduction dynamics of the western Pacific plate, and the mantle flow pattern and tectonic evolution in East Asia. Main findings of the present study are summarized as follows.

1. The low-V mantle under the Pacific slab beneath the Japan arc mainly exhibits subduction-parallel FVDs at depths of 160–400 km but subduction-normal FVDs in the MTZ and uppermost lower mantle. This result may reflect 2-D subduction-parallel subslab mantle flow in the upper mantle but subduction-normal subslab mantle flow that is decoupled from the subducting Pacific slab in the MTZ and uppermost lower mantle.
2. Trench-parallel FVDs are visible in the shallow portion of the subducting Pacific slab (<80-km depth), whereas the deeper portion of the Pacific slab (~160–400-km depth) mainly exhibits trench-normal FVDs, except for the hinge part of stagnant Pacific slab in the MTZ where obvious NE-SW (trench-parallel) FVDs are revealed.
3. Obvious toroidal FVDs and low-V anomalies exist in and around the Izu-Bonin arc and the Philippine Sea plate, which may reflect toroidal mantle flow resulting from a Pacific slab tear below 300-km depth at the junction of the Japan and Izu-Bonin slabs.
4. The high-V anomalies in the MTZ under East China reflect the same stagnant Pacific slab rather than several segmented slab structures. The flat slab now in the MTZ is the subducted Pacific slab initiating in the Paleocene rather than the Izanagi slab.
5. The Cenozoic intraplate volcanoes in Northeast Asia are not hot spots related to deep mantle plumes but caused by hot and wet upwelling flows in the BMW associated with the deep subduction of the western Pacific plate.



6. The NE striking high-V structure beneath the western part of the Yangtze Craton reflects the subducting Burma microplate and/or the Indian plate. The active Tengchong volcano in SW China is caused by the BMW processes above the stagnant Burma or Indian slab in the MTZ.

#### Acknowledgments

This work was supported by grants from the National Natural Science Foundation of China (Grants 41430322 and 41474030) to Y. Tian, a grant from Japan Society for the Promotion of Science (19H01996) to D. Zhao, and the China Scholarship Council to J. Ma and T. Liu (CSC201806170051 and CSC201806170055). Part of the work was done when J. Ma was a graduate student at Jilin University. We thank the International Seismological Center (<http://www.isc.ac.uk/iscbulletin/search/arrivals/>), the China Earthquake Data Center (<http://data.earthquake.cn>), and the Japanese Kiban Seismic Network (<http://www.hinet.bosai.go.jp>) for providing the high-quality arrival time data used in this study. All the data used for this study are archived on the webpage: <https://zenodo.org/record/3237008#.XPmNXogzY2w>. We appreciate the fruitful discussions with Profs. Wenliang Xu, Dicheng Zhu, and Jianbo Zhou. We thank Dr. Chuanxu Chen for helping us make Figure 14 with ParaView (<http://www.paraview.org>). The free software GMT (Wessel & Smith, 1998) is used for making most of the figures. We are very grateful to Prof. Maureen Long (the Editor), Prof. Tuna Eken, and an anonymous reviewer for their thoughtful review comments and suggestions, which have greatly improved this paper.

#### References

- Amaru, M. L. (2007). *Global travel time tomography with 3-D reference models*. PhD thesis. the Netherlands: Utrecht University.
- Ando, M., Ishikawa, Y., & Yamazaki, F. (1983). Shear wave polarization anisotropy in the upper mantle beneath Honshu, Japan. *Journal of Geophysical Research*, *88*(B7), 5850–5864. <https://doi.org/10.1029/JB088iB07p05850>
- Anglin, D., & Fouch, M. (2005). Seismic anisotropy in the Izu-Bonin subduction system. *Geophysical Research Letters*, *32*, L09307. <https://doi.org/10.1029/2005GL022714>
- Backus, G. (1965). Possible forms of seismic anisotropy of the uppermost mantle under oceans. *Journal of Geophysical Research*, *70*(14), 3429–3439. <https://doi.org/10.1029/JZ070i014p03429>
- Balmino, G., Vales, N., Bonvalot, S., & Briais, A. (2012). Spherical harmonic modelling to ultra-high degree of Bouguer and isostatic anomalies. *Journal of Geodesy*, *86*(7), 499–520. <https://doi.org/10.1007/s00190-011-0533-4>
- Becker, T. W. (2011). In H. Gupta (Ed.), *Seismic anisotropy, in Encyclopedia of Solid Earth Geophysics*, (pp. 1070–1081). Dordrecht: Springer. [https://doi.org/10.1007/978-90-481-8702-7\\_51](https://doi.org/10.1007/978-90-481-8702-7_51)
- Becker, T. W., Lebedev, S., & Long, M. D. (2012). On the relationship between azimuthal anisotropy from shear wave splitting and surface wave tomography. *Journal of Geophysical Research*, *117*, B01306. <https://doi.org/10.1029/2011JB008705>
- Bijwaard, H., Spakman, W., & Engdahl, E. R. (1998). Closing the gap between regional and global travel time tomography. *Journal of Geophysical Research*, *103*(B12), 30055–30078. <https://doi.org/10.1029/98JB02467>
- Bird, P. (2003). An updated digital model of plate boundaries. *Geochemistry, Geophysics, Geosystems*, *4*(3), 1027. <https://doi.org/10.1029/2001GC000252>
- Bunge, H.-P., Hagelberg, C., & Travis, B. (2003). Mantle circulation models with variational data assimilation: Inferring past mantle flow and structure from plate motion histories and seismic tomography. *Geophysical Journal International*, *152*(2), 280–301. <https://doi.org/10.1046/j.1365-246X.2003.01823.x>
- Castellanos, J. C., Clayton, R. W., & Pérez-Campos, X. (2018). Imaging the eastern Trans-Mexican Volcanic Belt with ambient seismic noise: Evidence for a slab tear. *Journal of Geophysical Research: Solid Earth*, *123*, 7741–7759. <https://doi.org/10.1029/2018JB015783>
- Chen, C., Zhao, D., Tian, Y., Wu, S., Hasegawa, A., Lei, J., et al. (2017). Mantle transition zone, stagnant slab and intraplate volcanism in Northeast Asia. *Geophysical Journal International*, *209*, 68–85. <https://doi.org/10.1093/gji/ggw491>
- Chen, H., Niu, F., Obayashi, M., Grand, S. P., Kawakatsu, H., Chen, Y., et al. (2017). Mantle seismic anisotropy beneath NE China and implications for the lithospheric delamination hypothesis beneath the southern Great Xing'an rang. *Earth and Planetary Science Letters*, *471*, 32–41. <https://doi.org/10.1016/j.epsl.2017.04.030>
- Chen, Y., Li, W., Yuan, X., Badal, J. H., & Teng, J. (2015). Tearing of the Indian lithospheric slab beneath southern Tibet revealed by SKS-wave splitting measurements. *Earth and Planetary Science Letters*, *413*, 13–24. <https://doi.org/10.1016/j.epsl.2014.12.041>
- Christensen, U. (1995). Effects of phase transitions on mantle convection. *Annual Review of Earth and Planetary Sciences*, *23*(1), 65–87. <https://doi.org/10.1146/annurev.23.050195.000433>
- Civello, S., & Margheriti, L. (2004). Toroidal mantle flow around the Calabrian slab (Italy) from SKS splitting. *Geophysical Research Letters*, *31*, L10601. <https://doi.org/10.1029/2004GL019607>
- Colli, L., Ghelichkhan, S., Bunge, H.-P., & Oeser, J. (2018). Retrodictions of Mid Paleogene mantle flow and dynamic topography in the Atlantic region from compressible high resolution adjoint mantle convection models: Sensitivity to deep mantle viscosity and tomographic input model. *Gondwana Research*, *53*, 252–272. <https://doi.org/10.1016/j.gr.2017.04.027>
- Confal, J. M., Faccenda, M., Eken, T., & Taymaz, T. (2018). Numerical simulation of 3-D mantle flow evolution in subduction zone environments in relation to seismic anisotropy beneath the eastern Mediterranean region. *Earth and Planetary Science Letters*, *497*, 50–61. <https://doi.org/10.1016/j.epsl.2018.06.005>
- Crampin, S., & Chastin, S. (2003). A review of shear wave splitting in the crack-critical crust. *Geophysical Journal International*, *155*(1), 221–240. <https://doi.org/10.1046/j.1365-246X.2003.02037.x>
- Crampin, S., Chesnokov, E. M., & Hipkin, R. G. (1984). Seismic anisotropy—The state of the art: II. *Geophysical Journal of the Royal Astronomical Society*, *76*(1), 1–16. <https://doi.org/10.1111/j.1365-246X.1984.tb05017.x>
- DeMets, C., Gordon, R. G., Argus, D. F., & Stein, S. (1994). Effect of recent revisions to the geomagnetic reversal time scale on estimates of current plate motions. *Geophysical Research Letters*, *21*(20), 2191–2194. <https://doi.org/10.1029/94GL02118>
- Eakin, C. M., Long, M. D., Beck, S. L., Wagner, L. S., Tavera, H., & Condori, C. (2015). Upper mantle anisotropy beneath Peru from SKS splitting: Constraints on flat slab dynamics and interaction with the Nazca Ridge. *Earth and Planetary Science Letters*, *412*, 152–162. <https://doi.org/10.1016/j.epsl.2014.12.015>
- Eakin, C. M., Long, M. D., Scire, A., Beck, S. L., Wagner, L. S., Zandt, G., & Tavera, H. (2016). Internal deformation of the subducted Nazca slab inferred from seismic anisotropy. *Nature Geoscience*, *9*(1), 56–59. <https://doi.org/10.1038/ngeo2592>
- Eberhart-Phillips, D., & Henderson, C. M. (2004). Including anisotropy in 3-D velocity inversion and application to Marlborough, New Zealand. *Geophysical Journal International*, *156*(2), 237–254. <https://doi.org/10.1111/j.1365-246X.2003.02044.x>
- Eberhart-Phillips, D., & Reyners, M. (2009). Three-dimensional distribution of seismic anisotropy in the Hikurangi subduction zone beneath the central North Island, New Zealand. *Journal of Geophysical Research*, *114*, B06301. <https://doi.org/10.1029/2008JB005947>
- Engdahl, E. R., & Lee, W. H. R. (1976). Relocation of local earthquakes by seismic ray tracing. *Journal of Geophysical Research*, *81*(23), 4400–4406. <https://doi.org/10.1029/JB081i023p04400>
- Faccenda, M., Burlini, L., Gerya, T. V., & Mainprice, D. (2008). Fault-induced seismic anisotropy by hydration in subducting oceanic plates. *Nature*, *455*(7216), 1097–1100. <https://doi.org/10.1038/nature07376>
- Faccenda, M., & Capitanio, F. (2013). Seismic anisotropy around subduction zones: Insights from three-dimensional modeling of upper mantle deformation and SKS splitting calculations. *Geochemistry, Geophysics, Geosystems*, *14*, 243–262. <https://doi.org/10.1002/ggge.20055>
- Faccenda, M., & Capitanio, F. A. (2012). Development of mantle seismic anisotropy during subduction-induced 3-D flow. *Geophysical Research Letters*, *39*, L11305. <https://doi.org/10.1029/2012GL051988>

- Fichtner, A., van Herwaarden, D.-P., Afanasiev, M., Simuté, S., Krischer, L., Çubuk-Sabuncu, Y., et al. (2018). The collaborative seismic Earth model: Generation 1. *Geophysical Research Letters*, *45*, 4007–4016. <https://doi.org/10.1029/2018GL077338>
- Fong, D. C. L., & Saunders, M. (2011). LSMR: An iterative algorithm for sparse least-squares problems. *SIAM Journal on Scientific Computing*, *33*(5), 2950–2971. <https://doi.org/10.1137/10079687X>
- Fouch, M. J., & Rondenay, S. (2006). Seismic anisotropy beneath stable continental interiors. *Physics of the Earth and Planetary Interiors*, *158*(2–4), 292–320. <https://doi.org/10.1016/j.pepi.2006.03.024>
- Fukao, Y., & Obayashi, M. (2013). Subducted slabs stagnant above, penetrating through, and trapped below the 660 km discontinuity. *Journal of Geophysical Research: Solid Earth*, *118*, 5920–5938. <https://doi.org/10.1002/2013JB010466>
- Fukao, Y., Widiyantoro, S., & Obayashi, M. (2001). Stagnant slabs in the upper and lower mantle transition region. *Review of Geophysics*, *39*(3), 291–323. <https://doi.org/10.1029/1999RG000068>
- Gorbatov, A., & Kennett, B. L. N. (2003). Joint bulk-sound and shear tomography for Western Pacific subduction zones. *Earth and Planetary Science Letters*, *210*(3–4), 527–543. [https://doi.org/10.1016/S0012-821X\(03\)00165-1](https://doi.org/10.1016/S0012-821X(03)00165-1)
- Gu, Y. J., Okeler, A., & Shultz, R. (2012). Tracking slabs beneath northwestern Pacific subduction zones. *Earth and Planetary Science Letters*, *331*–332, 269–280. <https://doi.org/10.1016/j.epsl.2012.03.023>
- Hayes, G. P., Wald, D. J., & Johnson, R. L. (2012). Slab 1.0: A three-dimensional model of global subduction zone geometries. *Journal of Geophysical Research*, *117*, B01302. <https://doi.org/10.1029/2011JB008524>
- Hearn, T. (1996). Anisotropic Pn tomography in the western United States. *Journal of Geophysical Research*, *101*(B4), 8403–8414. <https://doi.org/10.1029/96JB00114>
- Hiramatsu, Y., Ando, M., & Ishikawa, Y. (1997). ScS wave splitting of deep earthquakes around Japan. *Geophysical Journal International*, *128*(2), 409–424. <https://doi.org/10.1111/j.1365-246X.1997.tb01564.x>
- Ho, K. S., Chen, J. C., & Juang, W. S. (2000). Geochronology and geochemistry of late Cenozoic basalts from the Leiqiong area, southern China. *Journal of Asia Earth Sciences*, *18*(3), 307–324. [https://doi.org/10.1016/S1367-9120\(99\)00059-0](https://doi.org/10.1016/S1367-9120(99)00059-0)
- Holtzman, B. K., Kohlstedt, D. L., Zimmerman, M. E., Heidelbach, F., Hiraga, T., & Hustoft, J. (2003). Melt segregation and strain partitioning: Implications for seismic anisotropy and mantle flow. *Science*, *301*(5637), 1227–1230. <https://doi.org/10.1126/science.1087132>
- Huang, J., & Zhao, D. (2006). High-resolution mantle tomography of China and surrounding regions. *Journal of Geophysical Research*, *111*, B09305. <https://doi.org/10.1029/2005JB004066>
- Huang, Z., Wang, L., Xu, M., Ding, Z., Wu, Y., Wang, P., et al. (2015). Teleseismic shear-wave splitting in SE Tibet: Insight into complex crust and upper-mantle deformation. *Earth and Planetary Science Letters*, *432*, 354–362. <https://doi.org/10.1016/j.epsl.2015.10.027>
- Huang, Z., Wang, L., Zhao, D., Mi, N., & Xu, M. (2011). Seismic anisotropy and mantle dynamics beneath China. *Earth and Planetary Science Letters*, *306*(1–2), 105–117. <https://doi.org/10.1016/j.epsl.2011.03.038>
- Huang, Z., Wang, P., Zhao, D., Wang, L., & Xu, M. (2014). Three-dimensional P wave azimuthal anisotropy in the lithosphere beneath China. *Journal of Geophysical Research: Solid Earth*, *119*, 5686–5712. <https://doi.org/10.1002/2014JB010963>
- Huang, Z., & Zhao, D. (2013). Mapping P-wave azimuthal anisotropy in the crust and upper mantle beneath the United States. *Physics of the Earth and Planetary Interiors*, *225*, 28–40. <https://doi.org/10.1016/j.pepi.2013.10.003>
- Huang, Z., Zhao, D., & Liu, X. (2015). On the trade-off between seismic anisotropy and heterogeneity: Numerical simulations and application to Northeast Japan. *Journal of Geophysical Research: Solid Earth*, *120*, 3255–3277. <https://doi.org/10.1002/2014JB011784>
- Huang, Z., Zhao, D., & Wang, L. (2011). Frequency-dependent shear-wave splitting and multilayer anisotropy in Northeast Japan. *Geophysical Research Letters*, *38*, L08302. <https://doi.org/10.1029/2011GL046804>
- Ishise, M., & Oda, H. (2005). Three-dimensional structure of P-wave anisotropy beneath the Tohoku district, northeast Japan. *Journal of Geophysical Research*, *110*, B07304. <https://doi.org/10.1029/2004JB003599>
- Ita, J., & Stixrude, L. (1992). Petrology, elasticity, and composition of the mantle transition zone. *Journal of Geophysical Research*, *97*(B5), 6849–6866. <https://doi.org/10.1029/92JB00068>
- Ito, E., & Takahashi, E. (1989). Postspinel transformations in the system Mg<sub>2</sub>SiO<sub>4</sub>-Fe<sub>2</sub>SiO<sub>4</sub> and some geophysical implications. *Journal of Geophysical Research*, *94*(B8), 10,637–10,646. <https://doi.org/10.1029/JB094iB08p10637>
- Jadamec, M., & Billen, M. (2010). Reconciling surface plate motions with rapid three-dimensional mantle flow around a slab edge. *Nature*, *465*(7296), 338–341. <https://doi.org/10.1038/nature09053>
- Jeanloz, R., & Thompson, A. B. (1983). Phase transitions and mantle discontinuities. *Review of Geophysics*, *21*(1), 51–74. <https://doi.org/10.1029/RG021i001p00051>
- Karato, S. (2008). *Deformation of Earth materials: Introduction to the rheology of the solid earth*, 463 pp. Cambridge: Cambridge University Press. <https://doi.org/10.1017/CBO9780511804892>
- Karato, S., Jung, H., Katayama, I., & Skemer, P. (2008). Geodynamic significance of seismic anisotropy of the upper mantle: New insights from laboratory studies. *Annual Review of Earth and Planetary Sciences*, *36*(1), 59–95. <https://doi.org/10.1146/annurev.earth.36.031207.124120>
- Karato, S., & Wu, P. (1993). Rheology of upper mantle: A synthesis. *Science*, *260*(5109), 771–778. <https://doi.org/10.1126/science.260.5109.771>
- Kawazoe, T., Ohuchi, T., Nashihara, Y., Nishiyama, N., Fujino, K., & Irifune, T. (2013). Seismic anisotropy in the mantle transition zone induced by shear deformation of wadsleyite. *Physics of the Earth and Planetary Interiors*, *216*, 91–98. <https://doi.org/10.1016/j.pepi.2012.12.005>
- Kennett, B. L. N., & Engdahl, E. R. (1991). Traveltimes for global earthquake location and phase identification. *Geophysical Journal International*, *105*(2), 429–465. <https://doi.org/10.1111/j.1365-246X.1991.tb06724.x>
- Kennett, B. L. N., & Furumura, T. (2010). Tears or thinning? Subduction structures in the Pacific plate beneath the Japanese Islands. *Physics of the Earth and Planetary Interiors*, *180*(1–2), 52–58. <https://doi.org/10.1016/j.pepi.2010.03.001>
- Kennett, B. L. N., & Gudmundsson, O. (1996). Ellipticity corrections for seismic phases. *Geophysical Journal International*, *127*(1), 40–48. <https://doi.org/10.1111/j.1365-246X.1996.tb01533.x>
- Kobayashi, K., Nakanishi, M., Tamaki, K., & Ogawa, Y. (1998). Outerslope faulting associated with the western Kuril and Japan trenches. *Geophysical Journal International*, *134*(2), 356–372. <https://doi.org/10.1046/j.1365-246x.1998.00569.x>
- Koulakov, I. (2011). High-frequency P and S velocity anomalies in the upper mantle beneath Asia from inversion of worldwide traveltimes data. *Journal of Geophysical Research*, *116*, B04301. <https://doi.org/10.1029/2010JB007938>
- Laske, G., G. Masters, Z. Ma and M. Pasyanos (2013), Update on CRUST1.0—A 1-degree global model of Earth's crust, *Geophys. Res. Abstracts*, *15*, Abstract EGU2013-2658, 2013.
- Lebedev, S., & Nolet, G. (2003). Upper mantle beneath Southeast Asia from S velocity tomography. *Journal of Geophysical Research*, *108*(B1), 2048. <https://doi.org/10.1029/2000JB000073>



- Lees, J., & Crosson, R. (1989). Tomographic inversion for three-dimensional velocity structure at Mount St. Helens using earthquake data. *Journal of Geophysical Research*, *94*(B5), 5716–5728. <https://doi.org/10.1029/JB094iB05p05716>
- Lei, J. (2012). Upper-mantle tomography and dynamics beneath the North China Craton. *Journal of Geophysical Research*, *117*, B06313. <https://doi.org/10.1029/2012JB009212>
- Lei, J., & Zhao, D. (2005). P-wave tomography and origin of the Changbai intraplate volcano in Northeast Asia. *Tectonophysics*, *397*(3–4), 281–295. <https://doi.org/10.1016/j.tecto.2004.12.009>
- Li, C., & van der Hilst, R. D. (2010). Structure of the upper mantle and transition zone beneath Southeast Asia from traveltimes tomography. *Journal of Geophysical Research*, *115*, B07308. <https://doi.org/10.1029/2009JB006882>
- Li, C., van der Hilst, R. D., Engdahl, E. R., & Burdick, S. (2008). A new global model for P wave speed variations in Earth's mantle. *Geochemistry, Geophysics, Geosystems*, *9*, Q05018. <https://doi.org/10.1029/2007GC001806>
- Liu, L., & Zhou, Q. (2015). Deep recycling of oceanic asthenosphere material during subduction. *Geophysical Research Letters*, *42*, 2204–2211. <https://doi.org/10.1002/2015GL063633>
- Liu, X., & Zhao, D. (2015). Seismic attenuation tomography of the Southwest Japan arc: New insight into subduction dynamics. *Geophysical Journal International*, *201*(1), 135–156. <https://doi.org/10.1093/gji/ggv007>
- Liu, X., & Zhao, D. (2016a). Seismic velocity azimuthal anisotropy of the Japan subduction zone: Constraints from P and S wave traveltimes. *Journal of Geophysical Research: Solid Earth*, *121*, 5086–5115. <https://doi.org/10.1002/2016JB013116>
- Liu, X., & Zhao, D. (2016b). Backarc spreading and mantle wedge flow beneath the Japan Sea: Insight from Rayleigh-wave anisotropic tomography. *Geophysical Journal International*, *207*(1), 357–373. <https://doi.org/10.1093/gji/ggw288>
- Liu, X., & Zhao, D. (2017). P-wave anisotropy, mantle wedge flow and olivine fabrics beneath Japan. *Geophysical Journal International*, *210*(3), 1410–1431. <https://doi.org/10.1093/gji/ggx247>
- Liu, X., Zhao, D., & Li, S. (2013). Seismic heterogeneity and anisotropy of the southern Kuril arc: Insight into megathrust earthquakes. *Geophysical Journal International*, *194*(2), 1069–1090. <https://doi.org/10.1093/gji/ggt150>
- Liu, X., Zhao, D., & Li, S. (2014). Seismic attenuation tomography of the Northeast Japan arc: Insight into the 2011 Tohoku earthquake ( $M_w$ 9.0) and subduction dynamics. *Journal of Geophysical Research: Solid Earth*, *119*, 1094–1118. <https://doi.org/10.1002/2013JB010591>
- Liu, X., Zhao, D., Li, S., & Wei, W. (2017). Age of the subducting Pacific slab beneath East Asia and its geodynamic implications. *Earth and Planetary Science Letters*, *464*, 166–174. <https://doi.org/10.1016/j.epsl.2017.02.024>
- Long, M. (2013). Constraints on subduction geodynamics from seismic anisotropy. *Review of Geophysics*, *51*, 76–112. <https://doi.org/10.1002/rog.20008>
- Long, M. D., & Silver, P. G. (2008). The subduction zone flow field from seismic anisotropy: A global view. *Science*, *319*(5861), 315–318. <https://doi.org/10.1126/science.1150809>
- Lynner, C., & Long, M. (2014a). Sub-slab anisotropy beneath the Sumatra and circum-Pacific subduction zones from source-side shear wave splitting observations. *Geochemistry, Geophysics, Geosystems*, *15*, 2262–2281. <https://doi.org/10.1002/2014GC005239>
- Lynner, C., & Long, M. (2014b). Testing models of sub-slab anisotropy using a global compilation of source-side shear wave splitting data. *Journal of Geophysical Research: Solid Earth*, *119*, 7226–7244. <https://doi.org/10.1002/2014JB010983>
- Ma, J., Tian, Y., Liu, C., Zhao, D., Feng, X., & Zhu, H. (2018). P-wave tomography of Northeast Asia: Constraints on the western Pacific plate subduction and mantle dynamics. *Physics of the Earth and Planetary Interiors*, *274*, 105–126. <https://doi.org/10.1016/j.pepi.2017.11.003>
- Maggi, A., Debayle, E., Priestley, K., & Barruol, G. (2006). Azimuthal anisotropy of the Pacific region, Earth Planet. *Earth and Planetary Science Letters*, *250*(1–2), 53–71. <https://doi.org/10.1016/j.epsl.2006.07.010>
- Mainprice, D. (2007). Seismic anisotropy of the deep Earth from a mineral and rock physics perspective. In G. Schubert (Ed.), *Treatise on geophysics*, (Vol. 2, pp. 437–492). Oxford: Elsevier. <https://doi.org/10.1016/B978-044452748-6.00045-6>
- Mainprice, D., & Silver, P. (1993). Interpretation of SKS-waves using samples from the sub-continental lithosphere. *Physics of the Earth and Planetary Interiors*, *78*(3–4), 257–280. [https://doi.org/10.1016/0031-9201\(93\)90160-B](https://doi.org/10.1016/0031-9201(93)90160-B)
- Mao, W., & Zhong, S. (2018). Slab stagnation due to a reduced viscosity layer beneath the mantle transition zone. *Nature Geoscience*, *11*(11), 876–881. <https://doi.org/10.1038/s41561-018-0225-2>
- Masson, D. G. (1991). Fault patterns at outer trench walls. *Marine Geophysical Research*, *13*(3), 209–225. <https://doi.org/10.1007/BF00369150>
- Miller, M. S., Kennett, B. L. N., & Toy, V. G. (2006). Spatial and temporal evolution of the subducting Pacific plate structure along the western Pacific margin. *Journal of Geophysical Research*, *111*, B02401. <https://doi.org/10.1029/2005JB003705>
- Müller, R. D., Sdrolias, M., Gaina, C., & Roest, W. R. (2008). Age, spreading rates, and spreading asymmetry of the world's ocean crust. *Geochemistry, Geophysics, Geosystems*, *9*, Q04006. <https://doi.org/10.1029/2007GC001743>
- Müller, R. D., Sdrolias, M., Gaina, C., Steinberger, B., & Heine, C. (2008). Long-term sea-level fluctuations driven by ocean basin dynamics. *Science*, *319*(5868), 1357–1362. <https://doi.org/10.1126/science.1151540>
- Müller, R. D., Seton, M., Zahirovic, S., Williams, S. E., Matthews, K. J., Wright, N. M., et al. (2016). Ocean basin evolution and global-scale plate reorganization events since Pangea breakup. *Annual Review of Earth and Planetary Sciences*, *44*(1), 107–138. <https://doi.org/10.1146/annurev-earth-060115-012211>
- Nakajima, J., Shimizu, J., Hori, S., & Hasegawa, A. (2006). Shear-wave splitting beneath the southwestern Kurile arc and northeastern Japan arc: A new insight into mantle return flow. *Geophysical Research Letters*, *33*, L05305. <https://doi.org/10.1029/2005GL025053>
- Nicolas, A. (1993). Why fast polarization directions of SKS seismic waves are parallel to mountain belts. *Physics of the Earth and Planetary Interiors*, *78*(3–4), 337–342. [https://doi.org/10.1016/0031-9201\(93\)90164-5](https://doi.org/10.1016/0031-9201(93)90164-5)
- Nicolas, A., & Christensen, N. I. (1987). Formation of anisotropy in upper mantle peridotites—A review. In K. Fuchs, & C. Froidevaux (Eds.), *Composition, structure and dynamics of the lithosphere-asthenosphere system*, (pp. 111–123). Washington D. C.: AGU.
- Niu, X., Zhao, D., Li, J., & Ruan, A. (2016). P wave azimuthal and radial anisotropy of the Hokkaido subduction zone. *Journal of Geophysical Research: Solid Earth*, *121*, 2636–2660. <https://doi.org/10.1002/2015JB012651>
- Obayashi, M., Yoshimitsu, J., & Fukao, Y. (2009). Tearing of stagnant slab. *Science*, *324*(5931), 1173–1175. <https://doi.org/10.1126/science.1172496>
- Obayashi, M., Yoshimitsu, J., Nolet, G., Fukao, Y., Shiobara, H., Sugioka, H., et al. (2013). Finite frequency whole mantle P wave tomography: Improvement of subducted slab images. *Geophysical Research Letters*, *40*, 5652–5657. <https://doi.org/10.1002/2013GL057401>
- Okada, T., Matsuzawa, T., & Hasegawa, A. (1995). Shear-wave polarization anisotropy beneath the north-eastern part of Honshu, Japan. *Geophysical Journal International*, *123*(3), 781–797. <https://doi.org/10.1111/j.1365-246X.1995.tb06890.x>
- Paige, C. C., & Saunders, M. A. (1982). LSQR: An algorithm for sparse linear equations and sparse least squares. *ACM Transactions on Mathematical Software (TOMS)*, *8*(1), 43–71. <https://doi.org/10.1145/355984.355989>

- Paul, A., Karabulut, H., Mutlu, A., & Salaün, G. (2014). A comprehensive and densely sampled map of shear-wave azimuthal anisotropy in the Aegean–Anatolia region. *Earth and Planetary Science Letters*, 389, 14–22. <https://doi.org/10.1016/j.epsl.2013.12.019>
- Piromallo, C., Becker, T., Funicello, F., & Faccenna, C. (2006). Three-dimensional instantaneous mantle flow induced by subduction. *Geophysical Research Letters*, 33, L08304. <https://doi.org/10.1029/2005GL025390>
- Raitt, R., Shor, G. G., Francis, T. J. G., & Morris, G. B. (1969). Anisotropy of the Pacific upper mantle. *Journal of Geophysical Research*, 74(12), 3095–3109. <https://doi.org/10.1029/JB074i012p03095>
- Ringwood, A. E. (1975). *Composition and petrology of the Earth's mantle*. New York: McGraw-Hill.
- Rost, S., Garnero, E. J., & Williams, Q. (2008). Seismic array detection of subducted oceanic crust in the lower mantle. *Journal of Geophysical Research*, 113, B06303. <https://doi.org/10.1029/2007JB005263>
- Savage, M., Aoki, Y., Unglert, K., Ohkura, T., Umakoshi, K., Shimizu, H., et al. (2016). Stress, strain rate and anisotropy in Kyushu, Japan. *Earth and Planetary Science Letters*, 439, 129–142. <https://doi.org/10.1016/j.epsl.2016.01.005>
- Savage, M. K. (1999). Seismic anisotropy and mantle deformation: What have we learned from shear wave splitting? *Review of Geophysics*, 37(1), 65–106. <https://doi.org/10.1029/98RG02075>
- Seno, T., Stein, S., & Gripp, A. E. (1993). A model for the motion of the Philippine Sea Plate consistent with NUVEL-1 and geological data. *Journal of Geophysical Research*, 98(B10), 17,941–17,948. <https://doi.org/10.1029/93JB00782>
- Seton, M., Flament, N., Whittaker, J., Müller, R. D., Gurnis, M., & Bower, D. J. (2015). Ridge subduction sparked reorganization of the Pacific plate–mantle system 60–50 million years ago. *Geophysical Research Letters*, 42, 1732–1740. <https://doi.org/10.1002/2015GL063057>
- Shearer, P. M. (2009). *Introduction to seismology*, 396 pp. New York: Cambridge University Press. <https://doi.org/10.1017/CBO9780511841552>
- Silver, P. G. (1996). Seismic anisotropy beneath the continents: Probing the depths of geology. *Annual Review of Earth and Planetary Sciences*, 24(1), 385–432. <https://doi.org/10.1146/annurev.earth.24.1.385>
- Silver, P. G., & Chan, W. W. (1991). Shear wave splitting and subcontinental mantle deformation. *Journal of Geophysical Research*, 96(B10), 16,429–16,454. <https://doi.org/10.1029/91JB00899>
- Simmons, N. A., Myers, S. C., Johannesson, G., & Matzel, E. (2012). LLNL-G3Dv3: Global P wave tomography model for improved regional and teleseismic travel time prediction. *Journal of Geophysical Research*, 117, B10302. <https://doi.org/10.1029/2012JB009525>
- Stegman, D. R., Freeman, J., Schellart, W. P., Moresi, L., & May, D. (2006). Influence of trench width on subduction hinge retreat rates in 3-D models of slab rollback. *Geochemistry, Geophysics, Geosystems*, 7, Q03012. <https://doi.org/10.1029/2005GC001056>
- Takeuchi, N., Kawakatsu, H., Tanaka, S., Obayashi, M., Chen, Y. J., Ning, J., et al. (2014). Upper mantle tomography in the northwestern Pacific region using triplicated P waves. *Journal of Geophysical Research: Solid Earth*, 119, 7667–7685. <https://doi.org/10.1002/2014JB011161>
- Tang, Y., Obayashi, M., Niu, F., Grand, S. P., Chen, Y. J., Kawakatsu, H., et al. (2014). Changbaishan volcanism in northeast China linked to subduction-induced mantle upwelling. *Nature Geoscience*, 7(6), 470–475. <https://doi.org/10.1038/ngeo2166>
- Tao, K., Grand, S. P., & Niu, F. (2018). Seismic structure of the upper mantle beneath eastern Asia from full waveform seismic tomography. *Geochemistry, Geophysics, Geosystems*, 19, 2732–2763. <https://doi.org/10.1029/2018GC007460>
- Thurber, C. H. (1983). Earthquake location and three-dimensional crustal structure in the Coyote Lake area, Central California. *Journal of Geophysical Research*, 88(B10), 8226–8236. <https://doi.org/10.1029/JB088iB10p08226>
- Tian, Y., & Zhao, D. (2012). Seismic anisotropy and heterogeneity in the Alaska subduction zone. *Geophysical Journal International*, 190(1), 629–649. <https://doi.org/10.1111/j.1365-246X.2012.05512.x>
- Tian, Y., & Zhao, D. (2013). Reactivation and mantle dynamics of North China Craton: Insight from P-wave anisotropy tomography. *Geophysical Journal International*, 195(3), 1796–1810. <https://doi.org/10.1093/gji/ggt333>
- Tian, Y., Zhao, D., Sun, R., & Teng, J. (2009). Seismic imaging of the crust and upper mantle beneath the North China Craton. *Physics of the Earth and Planetary Interiors*, 172(3–4), 169–182. <https://doi.org/10.1016/j.pepi.2008.09.002>
- Tian, Y., Zhu, H., Zhao, D., Liu, C., Feng, X., Liu, T., & Ma, J. (2016). Mantle transition zone structure beneath the Changbai volcano: Insight into deep slab dehydration and hot upwelling near the 410 km discontinuity. *Journal of Geophysical Research: Solid Earth*, 121, 5794–5808. <https://doi.org/10.1002/2016JB012959>
- Tibi, R., Wiens, D. A., Shiobara, H., Sugioka, H., & Shore, P. J. (2006). Depth of the 660-km discontinuity near the Mariana slab from an array of ocean bottom seismographs. *Geophysical Research Letters*, 33, L02313. <https://doi.org/10.1029/2005GL024523>
- Tibi, R., Wiens, D. A., Shiobara, H., Sugioka, H., & Yuan, X. (2007). Double seismic discontinuities at the base of the mantle transition zone near the Mariana slab. *Geophysical Research Letters*, 34, L16316. <https://doi.org/10.1029/2007GL030527>
- Tono, Y., Fukao, Y., Kunugi, T., & Tsuboi, S. (2009). Seismic anisotropy of the Pacific slab and mantle wedge beneath the Japanese islands. *Journal of Geophysical Research*, 114, B07307. <https://doi.org/10.1029/2009JB006290>
- Um, J., & Thurber, C. (1987). A fast algorithm for two-point seismic ray tracing. *Bulletin of the Seismological Society of America*, 77, 972–986.
- Wang, J., Wu, H., & Zhao, D. (2014). P wave radial anisotropy tomography of the upper mantle beneath the North China Craton. *Geochemistry, Geophysics, Geosystems*, 15, 2195–2210. <https://doi.org/10.1002/2014GC005279>
- Wang, J., & Zhao, D. (2008). P-wave anisotropic tomography beneath northeast Japan. *Physics of the Earth and Planetary Interiors*, 170(1–2), 115–133. <https://doi.org/10.1016/j.pepi.2008.07.042>
- Wang, J., & Zhao, D. (2013). P-wave tomography for 3-D radial and azimuthal anisotropy of Tohoku and Kyushu subduction zones. *Geophysical Journal International*, 193(3), 1166–1181. <https://doi.org/10.1093/gji/ggt086>
- Wang, Z., Zhao, D., Liu, X., Chen, C., & Li, X. (2017). P and S wave attenuation tomography of the Japan subduction zone. *Geochemistry, Geophysics, Geosystems*, 18, 1688–1710. <https://doi.org/10.1002/2017GC006800>
- Wang, Z., Zhao, D., Liu, X., & Li, X. (2017). Seismic attenuation tomography of the source zone of the 2016 Kumamoto earthquake (M 7.3). *Journal of Geophysical Research: Solid Earth*, 122, 2988–3007. <https://doi.org/10.1002/2016JB013704>
- Wei, W., Hammond, J., Zhao, D., Xu, J., Liu, Q., & Gu, Y. (2019). Seismic evidence for a mantle transition zone origin of the Wudalianchi and Halaha volcanoes in northeast China. *Geochemistry, Geophysics, Geosystems*, 20, 398–416. <https://doi.org/10.1029/2018GC007663>
- Wei, W., Xu, J., Zhao, D., & Shi, Y. (2012). East Asia mantle tomography: New insight into plate subduction and intraplate volcanism. *Journal of Asia Earth Sciences*, 60, 88–103. <https://doi.org/10.1016/j.jseas.2012.08.001>
- Wei, W., Zhao, D., Xu, J., Wei, F., & Liu, G. (2015). P and S wave tomography and anisotropy in Northwest Pacific and East Asia: Constraints on stagnant slab and intraplate volcanism. *Journal of Geophysical Research: Solid Earth*, 120, 1642–1666. <https://doi.org/10.1002/2014JB011254>
- Wei, W., Zhao, D., Xu, J., Zhou, B., & Shi, Y. (2016). Depth variations of P-wave azimuthal anisotropy beneath Mainland China. *Scientific Reports*, 6(1), 29614. <https://doi.org/10.1038/srep29614>



- Wessel, P., & Smith, W. H. F. (1998). New, improved version of generic mapping tools released. *Eos, Transactions of the American Geophysical Union*, 79(47), 579–579. <https://doi.org/10.1029/98EO00426>
- Widiyantoro, S., Kennett, B., & van Der Hilst, R. (1999). Seismic tomography with P and S data reveals lateral variations in the rigidity of deep slabs. *Earth and Planetary Science Letters*, 173(1-2), 91–100. [https://doi.org/10.1016/S0012-821X\(99\)00216-2](https://doi.org/10.1016/S0012-821X(99)00216-2)
- Wirth, E., & Long, M. (2010). Frequency-dependent shear wave splitting beneath the Japan and Izu-Bonin subduction zones. *Physics of the Earth and Planetary Interiors*, 181(3-4), 141–154. <https://doi.org/10.1016/j.pepi.2010.05.006>
- Wu, J., Suppe, J., Lu, R., & Kanda, R. (2016). Philippine Sea and East Asian plate tectonics since 52 Ma constrained by new subducted slab reconstruction methods. *Journal of Geophysical Research: Solid Earth*, 121, 4670–4741. <https://doi.org/10.1002/2016JB012923>
- Wüstefeld, A., Bokelmann, G. H. R., Barruol, G., & Montagner, J.-P. (2009). Identifying global seismic anisotropy patterns by correlating shear-wave splitting and surface waves data. *Physics of the Earth and Planetary Interiors*, 176(3-4), 198–212. <https://doi.org/10.1016/j.pepi.2009.05.006>
- Xia, S., Zhao, D., Sun, J., & Huang, H. (2016). Teleseismic imaging of the mantle beneath southernmost China: New insights into the Hainan plume. *Gondwana Research*, 36, 33–43. <https://doi.org/10.1016/j.gr.2016.05.003>
- Xu, Y. (2007). Diachronous lithospheric thinning of the North China Craton and formation of the Daxin'anling–Taihangshan gravity lineament. *Lithos*, 96(1-2), 281–298. <https://doi.org/10.1016/j.lithos.2006.09.013>
- Xu, Y., Li, H., Hong, L., Ma, L., Ma, Q., & Sun, M. (2018). Generation of Cenozoic intraplate basalts in the big mantle wedge under eastern Asia. *Science China Earth Sciences*, 61(7), 869–886. <https://doi.org/10.1007/s11430-017-9192-y>
- Zandt, G., & Humphreys, E. (2008). Toroidal mantle flow through the western U.S. slab window. *Geology*, 36(4), 295–298. <https://doi.org/10.1130/G24611A.1>
- Zhang, M., Guo, Z., Liu, J., Liu, G., Zhang, L., Lei, M., et al. (2018). The intraplate Changbaishan volcanic field (China/North Korea): A review on eruptive history, magma genesis, geodynamic significance, recent dynamics and potential hazards. *Earth Science Reviews*, 187, 19–52. <https://doi.org/10.1016/j.earscirev.2018.07.011>
- Zhao, D. (2004). Global tomographic images of mantle plumes and subducting slabs: Insight into deep Earth dynamics. *Physics of the Earth and Planetary Interiors*, 146(1-2), 3–34. <https://doi.org/10.1016/j.pepi.2003.07.032>
- Zhao, D. (2015). *Multiscale seismic tomography*, 304 pp. Tokyo: Springer. <https://doi.org/10.1007/978-4-431-55360-1>
- Zhao, D., Fujisawa, M., & Toyokuni, G. (2017). Tomography of the subducting Pacific slab and the 2015 Bonin deepest earthquake ( $M_w 7.9$ ). *Scientific Reports*, 7, 44487. <https://doi.org/10.1038/srep44487>
- Zhao, D., Hasegawa, A., & Horiuchi, S. (1992). Tomographic imaging of P and S wave velocity structure beneath northeastern Japan. *Journal of Geophysical Research*, 97(B13), 19,909–19,928. <https://doi.org/10.1029/92JB00603>
- Zhao, D., Hasegawa, A., & Kanamori, H. (1994). Deep structure of Japan subduction zone as derived from local, regional, and teleseismic events. *Journal of Geophysical Research*, 99(B11), 22,313–22,329. <https://doi.org/10.1029/94JB01149>
- Zhao, D., & Tian, Y. (2013). Changbai intraplate volcanism and deep earthquakes in East Asia: A possible link? *Geophysical Journal International*, 195(2), 706–724. <https://doi.org/10.1093/gji/ggt289>
- Zhao, D., Tian, Y., Lei, J., Liu, L., & Zheng, S. (2009). Seismic image and origin of the Changbai intraplate volcano in East Asia: Role of big mantle wedge above the stagnant Pacific slab. *Physics of the Earth and Planetary Interiors*, 173(3-4), 197–206. <https://doi.org/10.1016/j.pepi.2008.11.009>
- Zhao, D., Yu, S., & Liu, X. (2016). Seismic anisotropy tomography: New insight into subduction dynamics. *Gondwana Research*, 33, 24–43. <https://doi.org/10.1016/j.gr.2015.05.008>
- Zhao, L., & Xue, M. (2010). Mantle flow pattern and geodynamic cause of the North China Craton reactivation: Evidence from seismic anisotropy. *Geochemistry, Geophysics, Geosystems*, 11, Q07010. <https://doi.org/10.1029/2010GC003068>